Optical Fiber Technology 18 (2012) 349–374

Contents lists available at SciVerse ScienceDirect

Optical Fiber Technology

www.elsevier.com/locate/yofte

Invited Papers

Modulation instability initiated high power all-fiber supercontinuum lasers and their applications

Vinay V. Alexander [a,*], Ojas P. Kulkarni [a], Malay Kumar [a], Chenan Xia [a], Mohammed N. Islam [a,b,d], Fred L. Terry Jr. [a], Michael J. Welsh [a,c], Kevin Ke [d], Michael J. Freeman [d], Manickam Neelakandan [e], Allan Chan [e]

[a] Electrical and Computer Engineering Department, University of Michigan, Ann Arbor, MI 48109, USA
[b] Department of Internal Medicine, University of Michigan Medical School, Ann Arbor, MI 48109, USA
[c] Department of Cell and Developmental Biology, University of Michigan, Ann Arbor, MI 48109, USA
[d] Omni Sciences Inc., Dexter, MI 48105, USA
[e] US Army CERDEC I2WD, Aberdeen Proving Ground, MD 21005, USA

ARTICLE INFO

Article history:
Available online 27 August 2012

Keywords:
Supercontinuum
Mid-infrared
Fiber
ZBLAN
Modulation instability

ABSTRACT

High average power, all-fiber integrated, broadband supercontinuum (SC) sources are demonstrated. Architecture for SC generation using amplified picosecond/nanosecond laser diode (LD) pulses followed by modulation instability (MI) induced pulse breakup is presented and used to demonstrate SC sources from the mid-IR to the visible wavelengths. In addition to the simplicity in implementation, this architecture allows scaling up of the SC average power by increasing the pulse repetition rate and the corresponding pump power, while keeping the peak power, and, hence, the spectral extent approximately constant. Using this process, we demonstrate >10 W in a mid-IR SC extending from ~0.8 to 4 μm, >5 W in a near IR SC extending from ~0.8 to 2.8 μm, and >0.7 W in a visible SC extending from ~0.45 to 1.2 μm. SC modulation capability is also demonstrated in a mid-IR SC laser with ~3.9 W in an SC extending from ~0.8 to 4.3 μm. The entire system and SC output in this case is modulated by a 500 Hz square wave at 50% duty cycle without any external chopping or modulation. We also explore the use of thulium doped fiber amplifier (TDFA) stages for mid-IR SC generation. In addition to the higher pump to signal conversion efficiency demonstrated in TDFAs compared to erbium/ytterbium doped fiber amplifier (EYFA), the shifting of the SC pump from ~1.5 to ~2 μm is pursued with an attempt to generate a longer extending SC into the mid-IR. We demonstrate ~2.5 times higher optical conversion efficiency from pump to SC generation in wavelengths beyond 3.8 μm in the TDFA versus the EYFA based SC systems. The TDFA SC spectrum extends from ~1.9 to 4.5 μm with ~2.6 W at 50% modulation with a 250 Hz square wave. A variety of applications in defense, health care and metrology are also demonstrated using the SC laser systems presented in this paper.

1. Introduction

We demonstrate high power, all-fiber integrated, SC laser sources from the visible to the mid-IR (~0.45–4.5 μm) wavelengths following a common framework for the SC generation process. Our approach utilizes amplified picosecond/nanosecond laser diode pulses, which are broken down into shorter, higher peak power pulses through MI and then coupled into an SC generation fiber to achieve further spectral broadening. We show that the SC generation approach outlined in this paper allows for each stage to be customized for the required wavelength output, and enables the scalability of average power in the SC by increasing the repetition rate and the corresponding pump power in the amplifier stages. Using this process, we demonstrate >10 W in a mid-IR SC extending from ~0.8 to 4 μm, >5 W in a near IR SC extending from ~0.8 to 2.8 μm, and >0.7 W in a visible SC extending from ~0.45 to 1.2 μm. Modulation capability is also demonstrated in our mid-IR SC system, where the entire system and the SC output are modulated with a 500 Hz square wave at 50% duty cycle without any external signal modulation or chopping equipments. Also presented in this paper, is a high efficiency mid-IR SC system using a TDFA based power-amplifier stage. The TDFA based system generates a mid-IR SC extending out to ~4.5 μm, up to ~270 nm further in wavelength than the longest spectrum from EYFA based systems presented here. In addition, the TDFA system is seen to be ~2.5 times more efficient in generating mid-IR SC beyond

* Corresponding author. Address: 1301 Beal Avenue, Electrical and Computer Engineering, Ann Arbor, MI 48109, USA. Fax: +1 734 647 2718.
E-mail address: vinalex@umich.edu (V.V. Alexander).

1068-5200/$ - see front matter © 2012 Elsevier Inc. All rights reserved.
http://dx.doi.org/10.1016/j.yofte.2012.07.014

3.8 μm with respect to the amplifier pump powers, than the corresponding EYFA based systems. Finally, we demonstrate applications in spectroscopy, health care and metrology enabled by the broad bandwidth and the high power of the SC systems presented in this paper.

Supercontinuum generation describes the process by which narrow band optical pulses undergo substantial spectral broadening through the interplay of a number of nonlinear optical interactions in the medium, to yield a broadband spectrally continuous output. Since its first observation in bulk media by Alfano [1], SC generation has been studied extensively and numerous applications using SC have been proposed and demonstrated. Broadband SC generation in optical fibers have been of particular interest due to the unique advantages offered by their long optical interaction lengths, high nonlinearity, and potential applications in optical telecommunications. In addition fiber based SC lasers are potentially compact, reliable and robust, which make them attractive candidates over conventional bulk lasers sources for practical applications. With the development of mature gain fibers, high power pump diodes, optical fibers of various materials, geometries and dispersion profiles; it is now possible to construct a broadband SC fiber laser platform for almost any wavelength of interest from the UV to the mid-IR.

The use of picosecond and nanosecond pump pulse regimes with MI initiated SC generation has enabled the development of high average power, broad band SC sources. In addition, this pump regime provides easier access to a range of attractive SC properties such as a high degree of spectral flatness and relative simplicity in implementation compared to many SC systems that use mode-locked lasers. Fig. 1 illustrates our architecture for MI initiated SC generation and provides a platform for generating SC in multiple wavelength regions. We utilize this framework to demonstrate SC systems in the mid-IR, near-IR and the visible wavelengths by selecting the appropriate gain fiber and SC generation fiber. In addition to the simplicity of implementation, we demonstrate that this architecture for SC generation also allows for the scalability of the SC time averaged power by simply increasing the repetition rates and the pump power in the amplifier stages.

In each system, we begin with ~1.5 μm picosecond/nanosecond laser diode pulses that are amplified through a series of cascaded fiber amplifier stages. These amplified pulses are then launched into a length of SMF fiber, where interaction between the nonlinearity and anomalous dispersion breaks up the quasi-CW input pulses into a train of solitons through MI and significantly increases the peak power. Thus, while many SC lasers use mode-locked femtosecond lasers to achieve high peak powers, MI enables the use of long pulses from compact laser diode sources. The

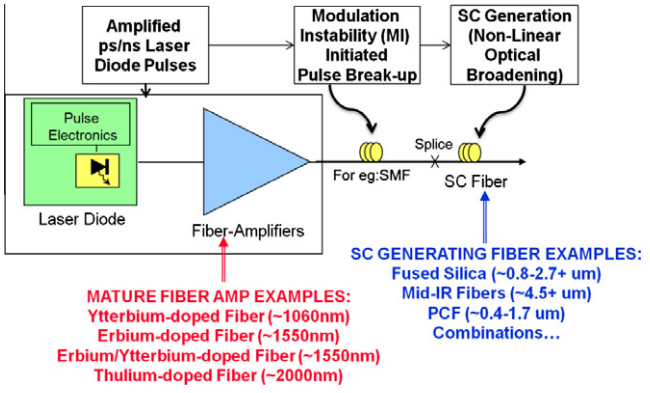

Fig. 1. Architecture for MI initiated SC generation process: amplified pump pulses followed by pulse breakup in single-mode fiber followed by spectral broadening in SC fiber.

generated solitons will undergo further spectral broadening in the SC fiber, due to a variety of nonlinear effects such as self phase modulation, soliton self frequency shift, Raman scattering and parametric four wave mixing. The SC fiber chosen depends on the SC wavelength requirements: photonic crystal fiber (PCF) following a frequency doubler for visible wavelengths, fused silica for near-IR wavelengths and ZBLAN for mid-IR wavelengths.

In this paper, we focus specifically on high power, all-fiber integrated mid-IR SC laser systems. A high power mid-IR SC source has a wide variety of applications, such as spectroscopy [2], IR countermeasures [3], free space communications [3], optical tissue ablation [4] to name a few. Conventional mid-IR laser sources including optical parametric amplifiers [5], quantum cascaded lasers [3], synchrotron lasers [6] and free electron lasers [7] have been used to demonstrate some of these applications. In comparison, an all-fiber, mid-IR SC laser has no moving parts, output in a single spatial mode and operate at room temperature. SC lasers also generate a broad spectrum covering the entire near IR and the mid-IR simultaneously, which can improve the selectivity of remote chemical sensing [8] and real time optical metrology [9]. In addition, direct signal modulation functionality is also desirable for SC laser sources to eliminate the need for external signal modulation or chopping equipments, which is difficult to implement in the mode-locked laser based systems. By initiating the SC generation through MI, we eliminate the need for a mode-locked laser in our SC systems and are able to use commercial off-the-shelf parts from the mature telecommunications and fiber optics industry.

The recent interest to incorporate a TDFA stage in a mid-IR SC laser is driven by the higher pump-to-signal conversion efficiency demonstrated in Tm-doped gain fibers compared to EYFAs. For example, slope efficiency as high as ~56% is demonstrated in Tm-doped gain fibers [10] compared to EYFAs, which have demonstrated slope efficiencies of ~38% in comparable fiber geometries [11]. Since the TDFA gain band is in the 1.9–2.1 μm region, a signal input at ~2 μm is required. Various techniques have been reported in the literature to generate ~2 μm pulses as input to the TDFA. For example, by using a mode-locked Er fiber laser with polarization maintaining components operating at 1557 nm followed by an EYFA, a Raman shifting soliton pulse to ~2 μm in a 12 m length of high NA fiber has been demonstrated by Imeshev and Fermann [12]. A subsequent dispersion-managed large mode area TDFA stage generates pulses with up to 230 kW peak power at ~2 μm. Another approach generates ~750 fs long ~1.95 μm pulses using a saturable absorber based carbon nanotubes in a Tm-doped fiber laser cavity [13]. Other approaches using 1.55 μm laser diode pulses, instead of mode-locked lasers have also been demonstrated. For instance, one approach involves three successive orders of cascaded Raman wavelength shifting from 1.53 μm to 1.94 μm in germanium-doped fused silica fibers with an NA of ~0.41 [14]. Another approach involves gain switching a Tm-doped fiber cavity with a modulated 1.55 μm pump to generate 10 ns long, 2 μm pulses [15]. In our approach, we first generate an SC extending across the thulium amplifier gain band, which is then further amplified in the TDFA power amp stage to act as a pump for further spectral broadening in the mid-IR. This is discussed in detail in Section 3.1.3.

This article is organized as follows. We begin with a brief literature review of recently reported SC sources. Then, in Section 3, we describe the SC experimental setups following the framework set in Fig. 1 and present the SC generation results for each of the wavelength regions. We first describe the high power mid-IR SC laser with ~10.5 W in an SC extending from ~0.8 to 4 μm. Then, we demonstrate a system where the power amp output peak power is scaled up to ~20 kW, to push the ZBLAN spectrum out further in wavelength to ~4.3 μm. Modulation capability is also demonstrated in this section. We then present the TDFA based high

efficiency mid-IR SC generation setup before briefly describing the near-IR and visible SC systems. Power scaling results are also included in this section, where we show that the SC average power can be scaled up by increasing the repetition rates and pump powers, while maintaining the peak power, and hence, the SC spectrum. Next, in Section 4, we present simulations to better explain and understand some of the SC results. Then, in Section 5, we present applications demonstrated using the SC laser systems presented in this paper. These include a system for stand-off detection of explosives and other solid targets and an atherosclerosis diagnosis and treatment tool, both using mid-IR SC lasers, a surface roughness measurement system using the near-IR SC system, a high resolution 3D interferometer system using the visible SC system, Finally, in Section 6, we discuss the experimental results, scopes and limitations of the SC systems before ending with our conclusions.

2. Literature overview

In this section, we briefly review some of the recent SC setups and results reported in the literature focusing more on the mid-IR SC regime. We also briefly describe the SC generation process relevant to the systems demonstrated in this paper. Table 1 provides a summary of the pump configuration, SC wavelength range and average power of the SC systems discussed in this section. The works presented here serve only to provide a background of some of the SC laser systems and is not an exhaustive list of reported SC sources. Detailed reviews of the works published with respect to continuum generation are provided by Dudley et al. [16], Genty et al. [17] and Taylor [18].

SC generation in optical fibers was first observed by Lin and Stolen for pumping in the normal group velocity dispersion regime in standard silica fiber, where the spectral broadening was attributed to a combination of Raman scattering, self- and cross-phase modulation and four wave mixing [19]. Since then, various groups have studied SC generation in silica fibers by pumping around 1310 nm, near the zero dispersion wavelengths, or around 1550 nm, in the anomalous dispersion region, where the spectral broadening was attributed mainly to soliton propagation dynamics. However, since most of the SC investigations were carried out in silica fibers, the long wavelength edge of the SC is generally <3 μm, which is then limited by the soaring absorption of silica glass [20]. In the past decade or so, fibers made of various materials, geometries and dispersion profiles have been investigated for SC generation and broadband SC has been reported in fibers covering the spectrum from the ultra-violet to the mid-IR.

SC generation in the visible wavelengths has been widely studied using photonic crystal fibers and various pump sources. For example mode-locked picoseconds pulses from a Yb fiber laser at 1060 nm have been used to generate >1 W in the visible region [21,22]. SC generation extending down to 400 nm was demonstrated using a microchip laser at 1064 nm to pump a PCF with modified group index in the IR to effectively phase match with deeper blue wavelengths [23]. Another method, as demonstrated by Kudlinski et al. uses tapers with continuously decreasing dispersion to generate SC with a wavelength edge at 400 nm and >2 mW/nm spectral density [24]. Multiple wavelength pumping schemes involving a pump and its second harmonic [25] or four wave mixing pump conversion [26] have also been demonstrated to increase spectral coverage in the visible region. Most of the techniques, however, use a mode-locked laser and suffer from one primary drawback, which is the lack of average power scalability due to a fixed repetition rate. SC systems based on microchip laser [26,27] and master oscillator power amplifier (MOPA) type pumps with the ability to vary repetition rates have been demonstrated. For example, Matos et al. demonstrated a repetition rate tunable chirped pulse amplification erbium system which was frequency doubled to generate SC in PCF with ~160 mW average power [28]. Kumar et al. demonstrated an SC extending from 0.45 to 1.2 μm with up to 0.74 W of time average power, by pumping a 1.5 m PCF with a frequency doubled, amplified, gain-switched, telecom laser diode [29] An advantage of the setup shown by Kumar et al. is that the average power can be scaled up from by increasing the repetition rate of the laser diode while keeping the peak power (and hence the spectral shape) constant. This result is discussed in Section 3.3. A detailed review of the ways to generate visible SC and to extend the short wavelength side of the SC further into the UV is given by Travers [30].

SC lasers in the IR have also been demonstrated in various pump and fiber configurations. Two approaches of generating SC are widely used: pumping a short length of nonlinear fiber using femtosecond pulses with high peak power, or using continuous

Table 1
Examples for SC sources with various pump and SC fiber configurations.

Pump configuration	SC fiber	SC wavelength	SC average power	Ref.
~600 ps, 1.064 μm, Q switched Nd:Yag microchip laser	PCF	~0.4–0.7 μm	–	[25]
600 ps, ~1.064 μm, Microchip laser	PCF	~0.4–2.45 μm	~12.4 mW	[23]
600 ps, ~1.064 μm, Q-switched Nd:Yag laser	PCF	~0.5 to >1.75 μm	<30 mW	[27]
~600 ps, 1.064 μm, Q-switched Nd:Yag microchip laser	PCF	~0.4 to >1.5 μm	<40 mW	[26]
1 ps, ~1.5 μm, Chirped-pulse amplification system	Photonic Bandgap Fiber	~0.43–1.45 μm	~0.16 W	[28]
~2 ns, 1,5 μm, DFB laser diode	PCF	~0.45–1.2 μm	~0.74 W	[29]
ps, 1.06 μm, Mode locked Yb fiber laser	PCF	~0.525–1.8 μm	>1.3 W	[21]
ps,1.06 μm, Mode locked Nd:glass oscillator	PCF	~0.5–1.8 μm	~5 W	[22]
~3–4 ps, 1.064 μm, Mode locked Yb pump laser	PCF	~0.37–1.75 μm	~3.5 W	[24]
30 ps, 1.55 μm, Gain-switched DFB laser	Dispersion shifted fiber	~0.9 to >1.8 μm	<50 mW	[32]
34 fs, 1.55 μm, Mode locked Er doped fiber laser	HiNL	0.85 to >2.6 μm	~0.4 W	[31]
CW, ~1.3 μm, Raman laser	HiNL	~1.2 to >1.7 μm	<~5 W	[34]
~2 ns, ~1.55 μm, DBR laser	HiNL	~0.8–2.8 μm	~5.3 W	[33]
CW, ~1.07 μm, Yb fiber laser	PCF	~1.06–1.67 μm	~29 W	[35]
~21 ps, ~1.06 μm, YDFA MOPA	PCF	~0.4–2.25 μm	~39 W	[36]
900 fs, 1.55 μm, Mode locked Er doped fiber laser	ZBLAN	~1.8–3.4 μm	~5 mW	[46]
100 fs, ~2.5 μm, OPA	Chalcogenide	~2.1–3.2 μm	–	[39]
110 fs, 1.55 μm, OPO	Soft-glass PCF	0.35–3 μm	~70 mW	[40]
100 fs, 1.55 μm OPO	Tellurite PCF	~0.79–4.87 μm	~70 mW	[41]
180 fs, 1.45 μm, Laser tunable OPA	ZBLAN	UV–6.28 μm	<20 mW	[47]
~2 ns, 1.55 μm, DFB laser diode	ZBLAN	~0.8–4.5 μm	~23 mW	[48]
~2 ns, 1.55 μm, DBR laser diode	ZBLAN	~0.8–4 μm	~1.3 W	[49]
~2 ns, 1.55 μm, DFB laser diode	ZBLAN	~1.9–4.5 μm	~5.2 W	[51]
0.4–2 ns, ~1.54 μm, DFB laser diode	ZBLAN	~0.8–4 μm	~10.5 W	[50]

wave (CW)/quasi-CW with lower peak power to pump longer lengths of fiber. For example, a mode-locked femtosecond erbium fiber laser was used to generate SC ranging from 0.8 to 2.7 μm in just 12 cm of highly nonlinear silica fiber [31]. Moon and Kim reported an SC extending from ~0.8 to 1.7 μm in dispersion shifted fiber using amplified laser diode pulses with 30 ps pulse width [32]. In contrast, Xia et al. reported a ~5.3 W SC ranging from ~0.8 to 3 μm in highly nonlinear silica fiber using nanosecond diode pulses amplified with a multistage amplifier [33]. This result is discussed further in Section 3.2. In the CW regime, Abeeluck and headley reported an SC generation extending beyond 1.75 um and ~5 W average output power in 500 m of highly nonlinear fibers pumped using a CW Raman fiber laser [34]. Ytterbium doped fiber amplifiers (YDFA) based pumps have also been used to demonstrate high power SC generation in silica based PCFs. For example, time average powers of ~29 W in an SC extending from 1.06 to 1.67 μm using a CW Ytterbium fiber laser has been demonstrated [35]. Time average powers of ~39 W in an SC extending from 0.4 to 2.25 μm using a picosecond YDFA MOPA pump source have also been reported [36]. Since, the pump wavelength is limited to ~1–1.2 μm for YDFA based pumps; the SC in this case extends out only to ~2.25 μm on the long wavelength side. In addition, since the pump wavelength for ytterbium based laser sources lie in the normal dispersion regimes for standard silica fibers, specialty dispersion engineered PCFs have to be used to utilize the advantages of pumping in the anomalous dispersion regime to obtain broader SC generation.

In order to generate SC in the mid-IR, optical fibers with low loss in the mid-IR windows, such as fluoride, chalcogenide and tellurite are required. For example, Sanghera et al. used a Ti:sapphire laser to generate 100-pJ, 100 fs duration pulses near 2.5 μm using nonlinear frequency conversion in bulk crystals; these pulses were coupled into various chalcogenide fibers to generate SC spanning ~2.1–3.2 μm (10 dB width) [37]. Kulkarni et al. reported spectral shifting from 1.55 μm to ~1.9 μm in chalcogenide fibers, where low optical damage threshold of ~1 GW/cm^2 and high normal GVD limits further red shifting of the spectrum [38]. Sulfide and selenide fibers have also been used to demonstrate SC ranging from 2 to 3 μm using a 2.5 μm OPA pump laser [39]. Omenetto et al. reported a broadband SC extending from 0.35 to beyond 3 μm in a short piece of high-nonlinearity soft glass PCF pumped using an OPO laser source that provides tunable femtosecond pulses around 1550 nm [40]. Domachuk et al. reported a broadband SC extending from ~0.79 to 4.87 μm, with ~90 mW of average output power by coupling 100 fs long, 1.55 μm pulses into an 8 mm length of highly nonlinear tellurite microstructured PCF fiber [41]. Various simulation results have also been reported where the fiber properties and dispersion profiles have been modified in non-silica fibers to generate mid-IR SC. Hu et al. published mid-IR SC generation results using chalcogenide PCFs with modified dispersion profiles [42]. Chen et al. showed simulations for generating coherent mid-IR SC in non-uniformly tapered ZBLAN fibers based on phase-matched dispersive wave generation by a soliton stabilized in the vicinity of a second zero dispersion wavelength [43]. Price et al. provided simulations showing the possibility of mid-IR SC generation in bismuth glass small core microstructured fibers by phase matching a 2 μm seed across the upper zero dispersion wavelength [44]. Thus, dispersion tailoring allows for the customization of the dispersion profiles in these fibers to generate broadband mid-IR SCs with the required spectral and coherence properties using easily available pump wavelengths. Lower dispersion can also be advantageous in broadband SC generation by reducing the peak intensity required for broadband SC generation.

Recently, ZBLAN fibers have been of great interest for SC generation in the mid-IR. Although, ZBLAN has a lower nonlinearity than that of silica, ZBLAN glasses are superior to other soft-glass fibers for high-power supercontinuum generation in the mid-IR due to their much lower background loss, relatively higher strength and a wide transparency window in the mid-IR region [45]. The first SC generation in ZBLAN fibers extending from ~1.8 to 3.4 μm, with a total average power of 5 mW, was demonstrated by Hagen et al., where a commercial mode locked, 1550 nm, Er3+ doped fiber laser with a 900 fs pulse duration and a repetition rate of 200 kHz was used to pump a 21 cm long standard single mode silica fiber. The output was then coupled to a ~91 cm long ZBLAN fiber with a core diameter of 8.5 μm and an NA of 0.21. SC generation in this case was based almost entirely on the cascaded Raman soliton self-shifting process [46]. Qin et al. demonstrated an ultra broadband SC generation expanding from the UV to ~6.28 μm where a 1450 nm femtosecond laser (20 mw average power, 50 MW peak power) with a pulse width of ~180 fs and repetition rate of ~1 kHz from a tunable OPA pumped by a Ti:sapphire femtosecond laser was launched into a 2 cm ZBLAN fiber. Since, the pump wavelength is in the normal dispersion region, initial spectral broadening is caused mainly by SPM and further spectral broadening occurs due to SPM, Raman scattering and four wave mixing [47]. Thus, femtosecond lasers have been used to generate SC beyond 3 μm using both fluoride and tellurite fibers, but with modest average powers (<0.1 W).

In contrast to ZBLAN SCs generated with femtosecond pump pulses, nanosecond pump pulses can be readily amplified using multiple fiber amplifier stages before the peak power related damage becomes of concern. This allows for the scalability in the total average power of the SC, enabled by the recent advances in high-power fiber amplifiers and fiber coupled laser diode pumps. The possible disadvantage, may be that the confinement loss is higher due to the longer lengths of ZBLAN required and the spectrum does not extend out as far as in the case of femtosecond pulses. A novel technique to eliminate the need for a mode-locked setup for high peak power pulse generation has been previously demonstrated by Xia et al. [33]. In this technique, MI in standard SMF is used to initiate pulse breakup of quasi-CW laser diode pulses to form shorter pulses with high peak powers. Xia et al. have demonstrated SC generation in ZBLAN fibers, extending from ~0.8 to 4.5 μm with an average power of ~23 mW [48]. They have also demonstrated the linear scaling up of the time-average power to 5.3 W [49] and then up to 10.5 W in a continuum extending from ~0.8 to 4 μm in ZBLAN fibers, using more powerful amplifier stages and higher repetition rates [50]. These results are discussed further in Section 3.1. Recently, Kulkarni et al. demonstrated a mid-IR SC laser, using a TDFA based system, extending from ~1.9 to 4.5 μm and total power of ~2.6 W in the SC, with ~0.7 W of time averaged power in wavelengths beyond 3.8 μm [51]. The SC in this case, is also modulated at 50% duty cycle. These results are discussed further in Section 3.1. Geng et al. also recently demonstrated a TDFA based mid-IR SC with a lower average power, extending from ~1.7 to 4.2 μm using ZBLAN fibers and ~1.8–2.9 μm using chalcogenide fibers [52].

Supercontinuum generation mechanisms have also been extensively studied and a number of reviews have been written, devoted to understanding the physical processes involved [16,17,53–55]. Fig. 2 provides a summary of the dominant mechanisms for the different pulse and dispersion regimes as described in Genty et al. [17]. Here, we will only briefly cover the physical process relevant to the SC systems presented in this article, which is picosecond and larger pulses pumping in the anomalous dispersion regime. For this pulse regime, the initial soliton dynamics is different from the sub-picosecond case. For pulses of long durations with high peak power, the soliton order N, becomes very large ($N = (L_D/L_{NL})^{1/2} \gg 10$), where L_D and L_{NL} are the nonlinear and dispersion lengths respectively. In this case, the soliton fission mechanism becomes less prominent. This is expected, since the characteristic length

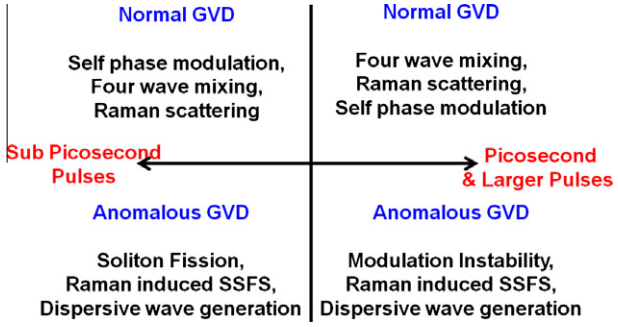

Fig. 2. Summary of dominant mechanisms for SC generation in different pulse and dispersion regimes.

scale over which fission occurs, $L_{fiss} = L_D/N \propto \Delta\tau$ and increases with pulse duration $\Delta\tau$ [16,56]. Instead, MI occurs and begins to dominate the initial soliton propagation mechanism. MI is the equivalent of parametric sidebands generated by four wave mixing and occurs on the same characteristic length scale, $L_{MI} = L_{NL}/2$ [53], independent of the pulse duration. In the time domain, this is characterized by the splitting of the pulse into shorter temporal sub-pulses.

The frequency shift of the first order MI gain peaks from the pump is given by $\Delta\omega_{MI} = \sqrt{2\gamma P/|\beta_2|}$, where γ is the nonlinearity coefficient, P is the pump peak power and β_2 is the group velocity dispersion parameter of the fiber at the pump wavelength [53]. The MI time period is then given by $T_{MI} = 2\pi/(\Delta\omega_{MI})$ and is the deciding factor for whether soliton fission or MI dominates the initial SC generation process. MI is expected to occur if the MI time period is sufficiently smaller than the pump pulse duration. Since the time period is a function of peak power, a specific pump pulse duration, below which fission occurs, cannot be defined as such. However, due to the similarity in scaling, it can reasonably be defined in terms of the soliton order [30]. Travers [30] calculated $N \sim 22$ for the upper limit on N for soliton fission to occur and is close to value of $N \sim 15$ calculated by Genty et al. [17]. Dudley et al. calculated N to be ~10, above which soliton fission will be overcome by MI [16]. The $N \sim 10$–22 range is not an issue for ultra-short pulse sources such as the mode locked lasers, but for picoseconds and longer pulse sources with high peak powers, enough to generate supercontinuum, N would be much larger. Thus, we would not expect any soliton fission to occur in this case. It has further been pointed out by Travers [30], that the products of MI do not themselves undergo any soliton fission, since only fundamental solitons are created from MI. Once the MI dynamics breaks up the pump pulses into shorter duration sub-pulses, further spectral broadening follows the same mechanism as the short pump pulses, where by the short wavelength side is due to the solitons that excite dispersive waves in the normal dispersion region through four wave mixing and dispersive wave generation and the long wavelength generation is due to the Raman induce soliton self frequency shift (SSFS). Pumping too far in the anomalous dispersion region could, however, result in reduced spectral broadening since the initial MI dynamics does not generate sufficient bandwidth to effectively seed the dispersive wave transfer into the normal dispersion regime [17]. Thus, in order to achieve the broadest SC in the picosecond and larger pulse regime, we should use a pump wavelength in the anomalous dispersion regime but closer to the zero dispersion wavelength of the fiber.

Coherence properties of SCs have also been widely studied in the literature [17,57]. For the SC systems presented in this paper, which utilize picosecond and larger pulses, SC generation is initiated with a fast modulation of the pump envelope. In the anomalous dispersion case, this modulation can arise from MI and/or Raman scattering. In both cases, the modulation arises spontaneously from noise at frequencies that do not overlap with the pump bandwidth [17]. Thus, MI initiated SC, which is a noise seeded process destroys any temporal coherence the pump pulse may have possessed and is therefore incoherent [30].

3. Experimental setup and results

In this section, we present the experimental setups and results used to demonstrate MI initiated SC in various wavelength bands from the mid-IR to the visible. All setups follow the framework described in Fig. 1, consisting of amplified picosecond/nanosecond laser diode pulses, MI induced pulse breakup and finally, the SC generation fiber. The SC fiber in each system, is chosen depending on the SC wavelength requirements; ZBLAN for Mid-IR wavelengths, silica for Near IR wavelengths, and photonic crystal fibers for visible wavelengths.

For the SC systems presented in this section, there are basically three adjustable parameters, which are the pulse width, the repetition rate and the pump power. To obtain the maximum SC power and to generate the broadest spectrum, all three parameters must be optimized. The pulse width is set based on the following two criteria. First, the pulse width should be short enough to mitigate any transient thermal effects in the fiber. On the other hand, a nanosecond pulse scale is also preferable for the intra-pulse nonlinear interaction and spectrum broadening. Therefore, we drive our distributed feedback (DFB) LD with pulse width in the range of 0.4–2 ns. Furthermore, the pulse repetition rate couples with the pulse width to determine the duty cycle of the laser system. Since the DFB LD pulses remove the energy provided by the pump lasers of the power amplifier of the SC system in time between DFB pulses, the peak output power varies inversely with the pulse duty cycle for a fixed pump power supply. In other words, the peak output power increases with the reduction of the pulse repetition rate, i.e. pulse duty cycle and vice versa. Thus, by increasing the repetition rate and the pump power accordingly, we can maintain the peak power for the required spectral extent while scaling up the total average power in the SC.

3.1. Mid-IR SC generation

We begin with the high power setup, where the average power is scaled up to ~10.5 W in an SC extending from ~0.8 to 4 μm. Next, we push the spectrum out further to ~4.3 μm by increasing the power-amp output peak power to ~20 kW. Modulation capability is also demonstrated, where the entire system and the SC is modulated with a 500 Hz square wave at 50% duty cycle, without the need for any external modulation or chopping mechanism. Finally, we present the SC laser specifically for higher efficiency in generating mid-IR wavelengths (greater than ~3.8 μm) by incorporating a TDFA as the power-amp stage. As we will see in Section 3.1.3, the TDFA system is an extension of the three stage approach, where we start by generating a first stage SC extending out to ~2 μm to serve as the seed for the TDFA power amp. The amplified 2 μm light from the TDFA output is then coupled into the ZBLAN fiber to generate the second stage mid-IR SC out to ~4.5 μm.

3.1.1. High average power mid-IR SC system

The experimental setup used for high power mid-IR SC generation is shown in Fig. 3a [50]. A 10 mW DFB laser diode at 1542 nm is driven by electronic circuits to provide 400 ps to 2 ns pulses at variable repetition rates and serves as the seed. The optical pulses are amplified by three stages of fiber amplifiers: an EDFA pre-amplifier followed by EYFA mid-stage amplifier and power amplifier stages. The pre-amplifier uses a 1 m length of 4/125 μm

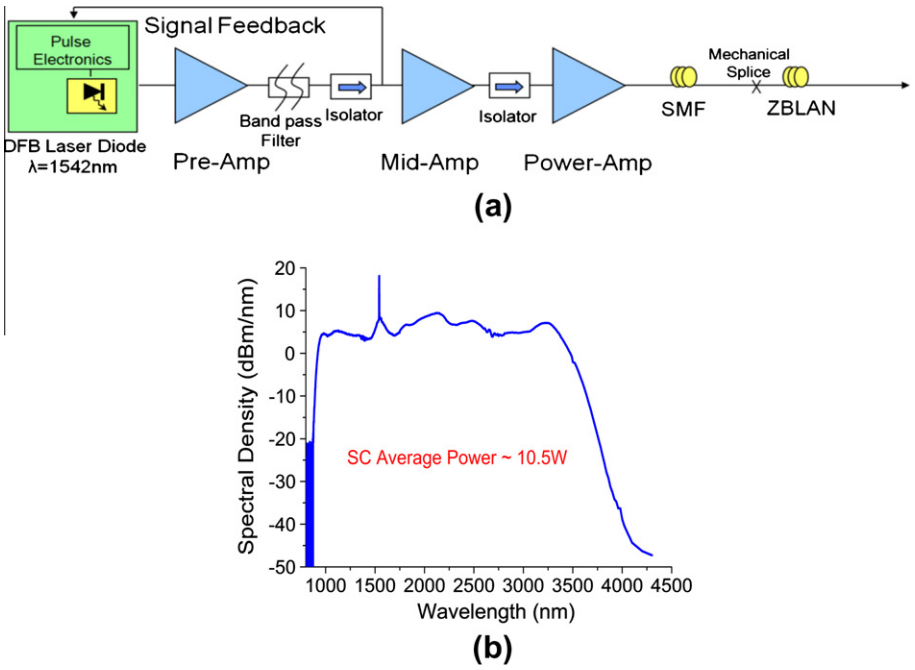

Fig. 3. (a) High power (10.5 W SC) all-fiber integrated SC laser setup. (b) SC spectrum for 2 m SMF followed by ~7 m ZBLAN fiber [50].

(core/cladding diameter) single mode EDFA, and the mid-amplifier stage uses a 1.5 m length of 7/125 (core/cladding diameter) cladding pumped gain fiber. To lower the ASE, the amplifier is separated into one pre-amplifier and one mid-amplifier and the ASE after the first stage is filtered by using a 100 GHz bandpass filter. Optical isolators are also placed between the stages to protect the system from any back reflection damage as well as to reduce the noise figure and improve the efficiency of the combined amplifier system. Under typical operating conditions, we obtain ~20 dB of gain in both the pre- and mid-amplifier stages for the optical signal, while the ASE to signal ratio is measured to be less than 1%. The power from the mid-amplifier is then boosted in an all-fiber spliced, cladding pumped EYFA before coupling into the SC fiber. A cladding pumped fiber amplifier increases the gain volume and enables the coupling of multiple pump diodes. In addition, to minimize the nonlinearity in the amplifier, we use 5 m of EYFA with 15/200 μm (core/cladding diameter) and a core NA of 0.15. Ten 8 W 976 nm diodes and two 8 W 940 nm uncooled multimode pump diodes are coupled into the gain fiber through an 18 × 1 combiner. Single spatial mode operation is maintained in the EYFA by carefully splicing the gain fiber to the signal-input SMF fiber and the pump combiner. By pumping the system with ~75 W average powers in the counter propagation configuration, the EYFA can provide ~20.2 W average power at the output of ~2 m SMF fiber that is spliced on to the power amp output. This corresponds to a peak power of ~6.1 kW (~15 dB signal gain) for 1 ns pulses at a 3.33 MHz repetition rate and ~27% pump-to-signal efficiency, which is slightly lower than the 30–35% value because of the high peak power induced nonlinear wavelength generation in both the fiber amplifier and the SMF. For the 10.5 W SC generation, the ZBLAN fiber used is 7 m long and has a core/cladding diameter of 8.9/125 μm and an NA of 0.21. The ends of the SMF and the ZBLAN fibers are both angle cleaved and clamped on to aluminum v-grooves before mechanically coupling them. The fiber cladding is also covered with high refractive index optical glue to strip out any residual cladding modes.

The output from the high power SC setup is shown in Fig. 3b. The SC spectrum extends from ~0.8 μm to beyond 4 μm, with a time averaged power of ~10.5 W in the continuum. The generated SC is smooth and relatively flat across majority of the spectrum with a spectral power density >0 dBm/nm (1 mW/nm). The SC average power beyond 1600, 2500, and 3000 nm is measured to be ~7.3 W, ~3.0 W, and ~1.1 W respectively, by using long-pass filters with the corresponding cutoff wavelengths. In the first stage SMF, we utilize MI to break up the nanosecond pulses into femtosecond pulses to enhance the nonlinear optical effects and redshifts the spectrum to beyond 2 μm. The SC spectrum is further broadened in the ZBLAN fiber through the interplay of SPM, Raman scattering and FWM. The long wavelength edge of the SC is limited by the input peak power and the length of the ZBLAN fiber in conjunction with other optical effects, including bend induced loss and material absorption.

The repetition rate must be optimized for maximum mid-IR power. For example, Fig. 4a shows the average power of the SC spectral components beyond 3 μm for varying pulse repetition rate with four 8 W 976 nm pump diodes. We see that the total SC spectral power beyond 3 μm increases from ~0.19 to ~0.48 W, by reducing the pulse repetition rate from 1.33 to 0.67 MHz. This increase of spectral power is attributed to the boost of the peak power coupled into the SMF and ZBLAN fibers to enhance the nonlinear SC generation process. However, we also see that the SC power drops down to ~0.26 W with further decrease in the repetition rate to 0.25 MHz. This drop in spectral power can be caused by the increased power loss in the SC long wavelength edge and reduced amplifier conversion efficiency. Since the SC long wavelength edge is limited by the loss of the fiber, the additional spectrum generated by the additional peak power is highly attenuated, which, in turn, reduces the total SC power in the mid-IR regime.

The time average power of the SC is seen to be linearly scalable with respect to the input pump power without changing the spectral shape. This is possible, since the entire SC spectrum is generated in each amplified nanosecond laser pulse, which does not interact with adjacent pulses, the SC average power can be boosted by simply increasing the number of optical pulses in a given time period, i.e. increase the repetition rate. To ensure that the SC spectrum, which is a function of the peak power, remains unchanged as the average power increases, it is necessary to boost the pump

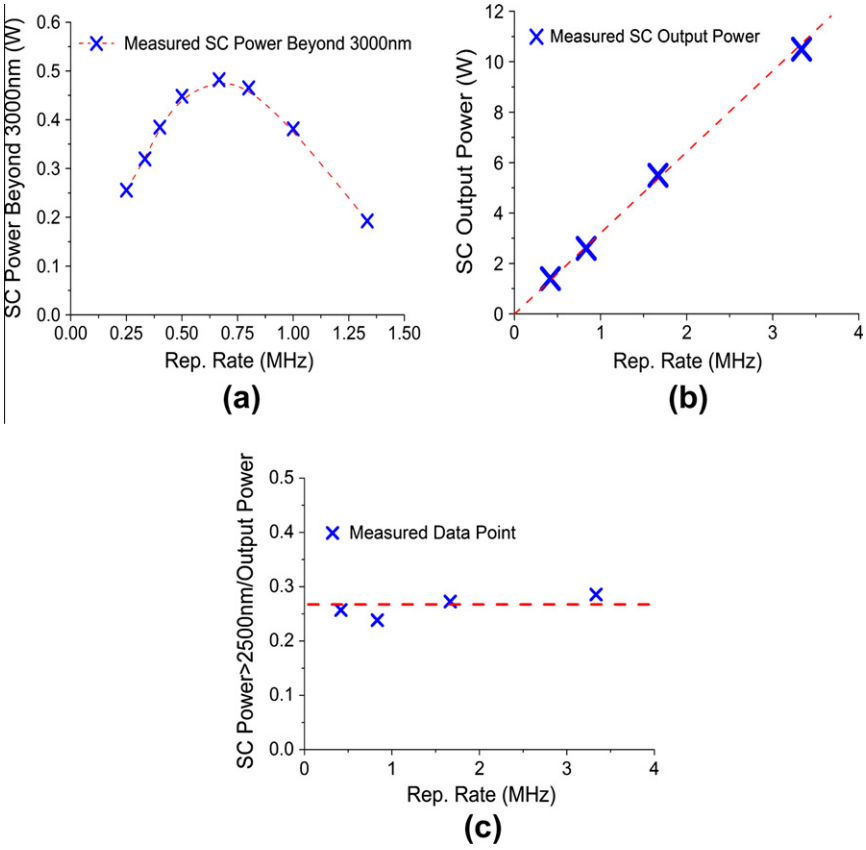

Fig. 4. (a) Average power of SC spectral components beyond 3 μm for varying pulse repetition rate with four 976 nm diodes. (B) Average SC power scaling by varying the pulse repetition rate and pump power. (c) Ratio of the SC power of the spectral components beyond 2.5 μm with respect to the total SC power under different operating repetition rates [50].

power as the repetition rate is increased, thus, keeping the peak power the same. As illustrated in Fig. 4b, we scale the SC average power from 1.4 to 10.5 W by varying the pulse repetition rate proportionally from 0.42 to 3.33 MHz and increasing the pump power accordingly. To further confirm that the SC spectrum remains unchanged as the total SC power is increased, the ratio of the SC spectral power beyond 2.5 μm over the total SC power is measured and shown in Fig. 4c. We observe that the ratio says approximately constant across the entire power range, which indicates that the power generated in the mid-IR scales up proportionally to the increasing total SC power. Therefore, the output power of our SC light source can be linearly and continuously varied with respect to the input pump power while keeping the same spectral shape.

3.1.2. Extending the SC wavelength edge

As seen in Fig. 3b, the ZBLAN SC output spectrum is seen to extend only to ~4 μm. In an effort to push the SC spectrum out further, we increase the peak power of the power-amp output from ~6 to 8 kW in the previous setup, to ~20 kW, and as a result see the wavelength edge of the SC extend further to ~4.3 μm. Additionally, we simplify the previous setup by using a single cladding pumped EYFA (12/130, core/cladding diameter) stage to combine the pre-amp and the mid-amp into a single pre-amp stage capable of providing sufficient signal gain. This setup is shown in Fig. 5a [2]. Modulation capability is also demonstrated in this setup, where the entire system is modulated at 500 Hz with a 50% duty cycle without any external chopping mechanism. The new pre-amp is pumped by a 10 W 976 nm diode. The power-amp uses the same EYFA as the previous setup. Four 25 W 976 nm multimode pump diodes are coupled into the gain fiber through a 6 × 1 combiner. At the highest 976 nm pump power of 52 W (104 W during ON phase), the 1543 nm signal output from ~1 m combiner fiber of the power-amp is ~9.6 W (19.2 W during the ON phase). This corresponds to a peak power of ~19.2 kW for 0.5 ns pulse at a 2 MHz repetition rate and ~19% pump to signal efficiency. The lower efficiency is again due to the higher peak power, which is responsible for spectral generation outside the gain band in the fiber amplifier. The output of the power-amp is then coupled into ~9 m ZBLAN with a core/cladding diameter of 8/125 μm and an NA of 0.27. Both the combiner fiber and the ZBLAN are angle cleaved and coupled using a mechanical fiber alignment stage.

The ZBLAN SC output corrected for the grating and detector response is shown in Fig. 5b and extends from ~0.75 to 4.3 μm with a time average power of ~3.9 W in the entire continuum, of which ~0.51 W lies in wavelengths beyond 3.8 μm. Since the system is modulated at 50% duty cycle, this corresponds to ~7.8 W in the continuum and ~1 W in wavelengths >3.8 μm during the ON phase of the modulation cycle. The modulated SC average power beyond 1800, 2500, and 3000 nm is measured to be ~2.7 W, ~2 W, and ~1.3 W respectively, by using long-pass filters with the corresponding cutoff wavelengths.

Power scalability is also shown in this system by increasing the repetition rate along with a proportional increase in the 976 nm pump power, while maintain the peak power going into the ZBLAN fiber. Fig. 5c shows the linear increase in the SC average output power with an increase in the seed laser repetition rate, with the corresponding 976 nm power-amp pump power labeled next to the data point. Further increase in output power is limited by the available pump power, and we expect the results to scale up with higher pump power and thermal management of the critical splice

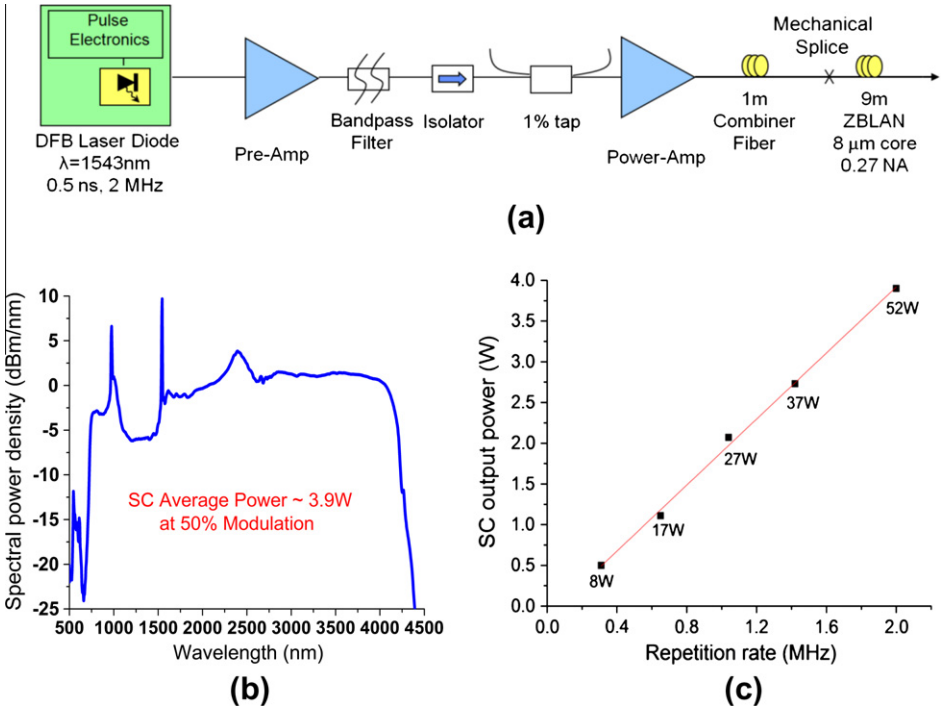

Fig. 5. (a) Setup for mid-IR SC generation in ZBLAN fiber with ~0.51 W (at 50% modulation) in wavelengths beyond 3.8 μm. (b) 3.9 W (at 50% modulation) SC output spectrum from the ZBLAN fiber. (c) SC output power scaling with repetition rate [2].

points and power-amp gain fiber. The wavelength edge in this set-up is now limited mainly by the inherent material absorption loss of the ZBLAN glass.

3.1.3. Improving mid-IR SC generation efficiency

For SC generation in wavelengths beyond ~2 μm into the mid-IR, a TDFA based SC laser is capable of providing a higher mid-IR (wavelengths > 3.8 μm) SC generation efficiency compared to EYFA based systems. We achieve this higher efficiency by incorporating a TDFA stage as the power-amp in our system. In our approach [51], as shown in Fig. 6a, the seed laser consists of a 1553 nm DFB laser diode with ~1 ns pulse output and a repetition rate adjustable from a few MHz down to ~10 kHz. The diode pulses are amplified to a peak power of a few kilowatts through the use of two EYFA stages pumped by ~980 nm diodes, in the pre-amp (2 m, 7/130 μm, core/cladding diameter, 400 mW pump) and the mid-amp stages (5 m, 12/130 μm, core/cladding diameter, 10 W pump), respectively. The output of the mid-amp is then spliced on to ~25 m SMF. This is the first SC generation stage, and is done in order to generate light in the Tm gain band, which extends from ~1.9 to 2.1 μm with a peak at 1.98 μm, for the power-amp stage. This first stage SC then serves as the seed for the power-amp that generates the high peak power input for the second stage SC output in the mid-IR. Although the first stage SC could be replaced with a seed laser near 2 μm in principle, we prefer to use the 1.55 μm seed stages, as this permits the use of standard off the shelf telecommunications technology.

The output of the 25 m SMF-based 2 μm light source is then spliced on to ~4.5 m of large mode area TDFA, which serves as the power-amp. The TDFA fiber has a core/cladding diameter of 25/250 μm, a low core NA of ~0.1 and is chosen to reduce the non-linear effects in the gain fiber. The mode conversion from ~10/125 to 25/250 μm, in this case is done using a pump combiner/mode adapter on both sides of the TDFA. Two 35 W 793 nm pump diodes are coupled into the gain fiber through a 6×1 combiner in the counter propagation configuration. The pumps are also modulated by a square wave with 50% duty cycle at ~250 Hz. The output of the TDFA is then mechanically spliced to the input end of ~8.5 m of ZBLAN fiber with a core/cladding diameter of 8/125 μm and an NA of ~0.27. The ZDW is expected to be ~1.65 μm based on the material dispersion parameter of ZBLAN [58]. The output of the ZBLAN fiber is measured with a thermal power meter, and a power distribution in various spectral bands is measured using suitable cutoff long pass filters. The spectrum is measured using a Czerny Turner monochromator and a TE-cooled HgCdTe detector.

The final SC output spectrum is shown in Fig. 6b and extends from ~1.9 to 4.5 μm, with a time averaged power of ~2.6 W in the continuum, of which ~0.7 W lies in wavelengths beyond 3.8 μm. The TDFA is pumped with ~30 W of 790 nm pump power modulated with a 50% duty cycle, 250 Hz square wave, and outputs ~8 W of average power around 2 μm. The input to the TDFA comprises the output from a ~25 m SMF with ~2.5 kW peak power 1.55 μm input pulses of ~1 ns duration at 500 kHz repetition rate. Once again, since the system is modulated, the observed SC output power of 2.6 W corresponds to ~5.2 W of SC output during the ON phase of the modulation signal, and the 0.7 W of average power measured beyond 3.8 μm indicates ~1.4 W of output during the ON phase. The dip in the spectrum at ~4.25 μm is attributed to the Co_2 absorption in the atmosphere while traversing the ~0.75 m path length inside the monochromator.

Fig. 6c shows the power scalability of the TDFA based mid-IR Sc laser as function of the pulse repetition rate and the 790 nm pump power. As can be seen, by varying the pulse repetition rate electronically, the Tm system shows versatility in its ability to adjust the output power with similar spectral extent. The spectrum out of the ZBLAN fiber is observed to have similar spectral extent and shape in each case; however, the average power is seen to scale linearly with the repetition rate. Thus, it is possible to increase the average power in the continuum by increasing the repetition rate and the pump power, while maintaining the pulse peak power. It is also seen that the amount of 790 nm pump power required to double the output average power with repetition rate

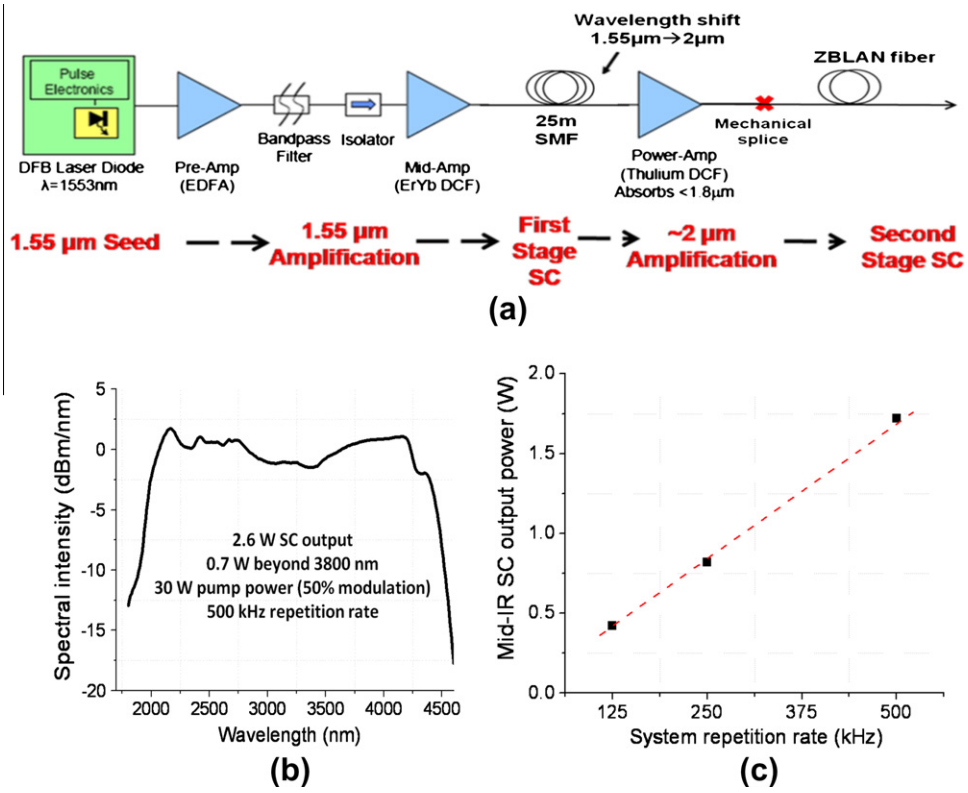

Fig. 6. (a) Experimental setup depicting two-stage mid-IR SC generation using thulium doped dual-cladding fiber. (b) Mid-IR SC spectrum, extending from ~1.9 to 4.5 μm from ~8.5 m ZBLAN fiber pumped with TDFA. (c) SC output power scaling with repetition rate [51].

does not scale linearly. For example, at 125 kHz, the SC outputs ~0.4 W average power at 12 W of modulated pump power. However, to double the output average power to ~0.8 W at 250 kHz, only ~3 W additional modulated pump power is required. The increase in efficiency with repetition rate is attributed to the threshold of the TDFA (~6 W) and the increase in the amplifier efficiency at higher pulse duty cycles, due to lower losses to spontaneous emission.

The first stage SC (output from the ~25 m SMF) must be optimized to obtain the broadest mid-IR SC at the output of the ZBLAN fiber. Fig. 7a shows the first stage SC spectra for various 1.55 μm pulse peak powers at the input of the 25 m of SMF. Fig. 7b shows the corresponding second stage SC measured at the output of ~12 m of ZBLAN for a fixed CW TDFA pump power of ~8 W. We observe that the lower input peak powers used for the 2 μm light generation gives the broadest ZBLAN output spectrum. However, the ASE peak from the TDFA in the ZBLAN output is higher for the lower peak power case due to insufficient strength of the input signal in the TDFA gain band. Therefore, even though the ZBLAN output spectrum extends further for the low peak power case, the efficiency of SC generation is poor compared to the high peak power case. We see that the higher spectral shifting efficiency (defined as the ratio of power in wavelengths >2.5 μm to the total SC power) is achieved at ~2.5 kW peak power compared to the lower peak powers, with saturation observed beyond 2 kW peak power. Above 2.5 kW, the standard SMF generates additional spectral components beyond 2.1 μm, which are not efficiently amplified in the TDFA. We discuss this further with simulations in Section 4.

Fig. 8 shows the modulated power measurements for varying 790 nm pump powers. The TDFA configuration shows an overall efficiency of ~27% with ~8 W output power at ~30 W of 790 nm pump power. The observed SC output power of ~2.6 W corresponds

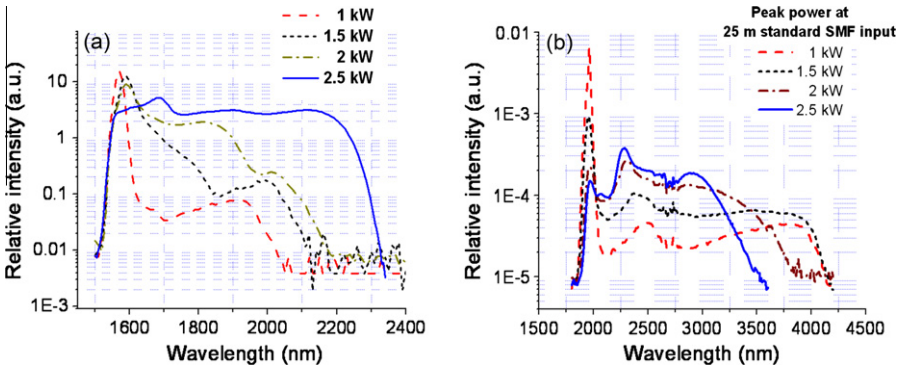

Fig. 7. Peak power optimization for stage 1 of the TDFA based SC source. (a) Output spectrum from ~25 m SMF for various peak input powers of 1.55 μm pulses. (b) Corresponding output spectrum from 12 m ZBLAN at ~8 W CW TDFA pump power for various 1.55 μm peak powers used in stage 1 [51].

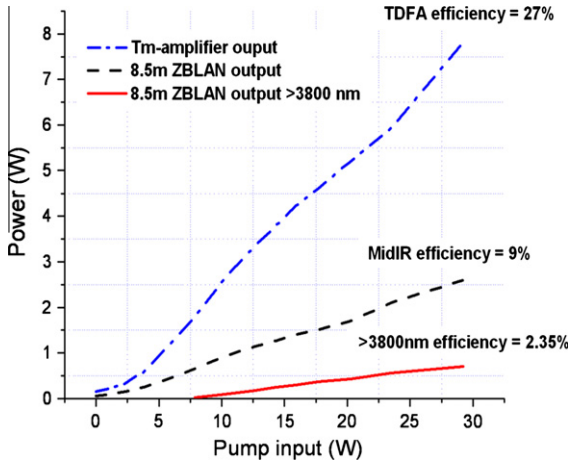

Fig. 8. Power measurements of the modulated TDFA output, ZBLAN SC output, and output average power >3.8 μm versus the 790 nm pump power [51].

to an overall mid-IR efficiency of ~9% with respect to the 790 nm pumps. ~0.7 W of the ZBLAN output lies in wavelengths beyond 3.8 μm, leading to an observed efficiency of ~2.35% in generating wavelengths >3.8 μm with respect to the TDFA pump power. We currently observe a 790 nm pump to 2 μm signal efficiency of ~27% for the TDFA system. However, this is lower than the absolute efficiency of ~53% demonstrated in a CW lasing cavity configuration in [10]. This discrepancy for our system is attributed to three main losses. First, the signal loss in the combiner-gain fiber splice and the insertion loss of the output combiner amounts up to ~1 dB of loss and accounts for ~7% reduction in the efficiency. In addition, the generation of high peak powers and the phonon losses associated with the spectral shifting process in the ~0.5 m length of the 10 μm core diameter fiber at the combined output, ~11% reduction is observed in the power-amp efficiency. Finally, the remainder of the gap is attributed to the low duty cycle of the input signal to the amplifier which results in larger losses to the spontaneous emission in the amplifier and reduces the efficiency of the system.

3.2. Near IR SC generation

In this section, we demonstrate one example of SC generation process in fused silica fibers following the same framework for the MI induced SC setups described in the previous sections. The near-IR SC light source extends from ~0.8 to 3 μm with a time averaged power of ~5.3 W in the continuum [33]. By using MI in the fiber, the broad spectrum is obtained with nanosecond pulses and a few meters of fused silica fiber. Fig. 9a shows the high power SC setup and consists of a distributed Bragg reflector LD producing 2 ns pulses that are amplified through three amplifier stages; 5.5 m of a standard single-mode EDFA based pre-amp pumped by a 320 mW, 1480 nm diode, an 8 m length of 7/130 μm core/cladding diameter EYFA based mid-amp and a 20 m long large mode area double clad EYFA based power-amp stage with a core/cladding diameter of 25/300 μm. The ASE of the first and second stage amplifiers is suppressed by using an acousto-optic modulator and a band pass filter. The power-amp in this case provides a free space output with 8.8 kW peak power (17.6 W average power) with ~80 W pump power, of which 3.8 kW peak power (7.6 W average power) is coupled into 3 m of single mode fiber which is then spliced on to ~1 m of highly nonlinear fiber (HiNL) to get the final SC output. The HiNL fiber used in the experiments has a ZDW of 1544 nm and a dispersion slope of 0.044 ps/(km nm^2). With an effective mode area of ~10 μm^2, the HiNL fiber has a nonlinearity coefficient of ~9.6 W^{-1} K m^{-1}.

The final SC output is shown in Fig. 9 b. The SC extends from ~0.8 to 2.8 μm, with a time average power of ~5.3 W in the continuum. The HiNL length is optimized experimentally to provide the broadest SC possible. We see that longer lengths merely attenuate the spectrum due to the high loss associated with the silica glass absorption around 3 μm, while shorter lengths do not provide

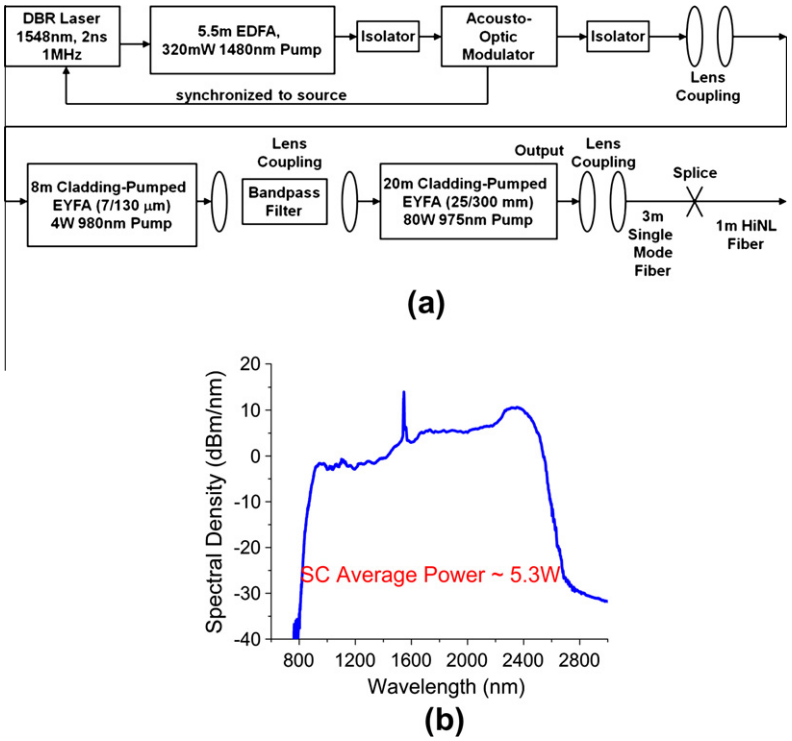

Fig. 9. (a) Experimental setup for near-IR SC generation: LD pulses amplified by cladding pumped EYFAs coupled into HiNL fiber. (b) Near-IR SC output spectrum [33].

sufficient nonlinearity to broaden the SC. Thus, obtaining the broadest spectrum requires the shortest fiber length, where the nonlinearity dominates over the loss.

The limit of the SC long wavelength edge, in this case can possibly be attributed to three factors; water absorption, bend induced loss, and the intrinsic silica glass absorption. Comparing the SC from dried fibers with non-dried fibers of 3–5 m lengths, the long wavelength edge extends ~100 nm and still does not go beyond ~2.8 μm, suggesting that water absorption is a factor, but not the dominant limitation. Fibers with different core sizes and similar index profiles also give comparable SC edges, which downplays the significance of the bend-induced loss. Finally, we measured the loss curve of the HiNL fiber [33], which shows that the intrinsic silica loss due to vibrational absorption is the limiting factor for the long wavelength edge of the SC. Thus, as we saw in the previous sections, fibers such as ZBLAN with lower loss in the mid-IR are required to extend the spectrum further out in wavelength.

With the understanding of SC generation characteristics and HiNL properties gained in this setup, we have scaled up the SC average power in an all-fiber HiNL based spectrum up to ~15 W using the setup for high power mid-IR SC generation, discussed in Section 3.1.1. In this case, we couple light of up to ~17 W average power (~6.3 kW peak power, 2 ns pulses) with a continuous spectrum from ~1.5 to 2 μm into a 0.4 m length of HiNL fiber [50] and scale up the power from ~2.4 to 15.2 W by increasing the repetition rate and the corresponding pump power. At the highest power level of ~15.2 W, we also observe a catastrophic backward propagating fiber fuse event starting from the HiNL fiber section after a short period of time. This is attributed to an average power induced damage event, where the fiber core temperature exceeded the melting temperature of silica glass. High power induced damage in fiber lasers is discussed further in Section 6.

3.3. Visible SC generation

Working in the opposite wavelength direction using the same SC generation framework, a block diagram of the visible SC setup is shown in Fig. 10a [29]. A 1553 nm DFB laser diode serves as the seed and is gain switched to produce 2 nanosecond (ns) pulses at variable repetition rates. The ns pulses are then amplified by two stages – a single mode EDFA pre-amp followed by a cladding pumped EYFA power-amp, pumped by two 976 nm laser diodes coupled into the gain fiber via a pump combiner. A 100 GHz band pass filter between the two amplifier stages is used to filter out the ASE. At the highest repetition rate of 1 MHz, the power-amp produces an output of 3.2 W average power (1.6 kW peak power). The power-amp output is spliced to a short length of SMF to allow for the MI induced pulse breakup of the 2 ns pulses into ultra short solitons. A quarter wave plate and a half wave plate are used at the output of the power-amp to adjust the polarization state of the light. This amplified 1553 nm pump system is then frequency doubled using a 10 mm long periodically poled Lithium Niobate (PPLN) crystal, which is temperature stabilized at 160 °C. The crystal temperature and the focused spot size in the PPLN crystal are optimized for maximum second harmonic generation efficiency. A thermal power meter and edge pass filters are used to measure the power in the fundamental (1553 nm) and the second harmonic (776.5 nm) wavelengths. The frequency doubled output at 776.5 nm from the PPLN acts as the pump source for the visible SC generation in the PCF. The light is then coupled into ~1.5 m of PCF (core diameter = 1.9 μm, λ_0 = 745 nm, dispersion slope at pump = 0.85 ps nm^{-2} K m^{-1}) using a 40× microscope objective with a coupling efficiency of ~50%. The output spectrum is then recorded using an optical spectrum analyzer with a 2 nm resolution.

The output spectrum from the PCF is shown in Fig. 10b. The continuum extends from ~0.45 to 1.2 μm with ~0.74 W time averaged power in the continuum. The spectrum is seen to have a spectral flatness of better than 2 dB in the 0.55 to 0.75 μm region. Apart from the peak at the pump wavelength, several additional peaks can be observed in the spectrum. The peak at ~518 nm is due to the third harmonic generation from the PPLN, while the peak at ~388 nm arises from the phase matched four wave mixing. The asymmetry in the spectral power density of the short and long wavelength regions arises due to the different continuum

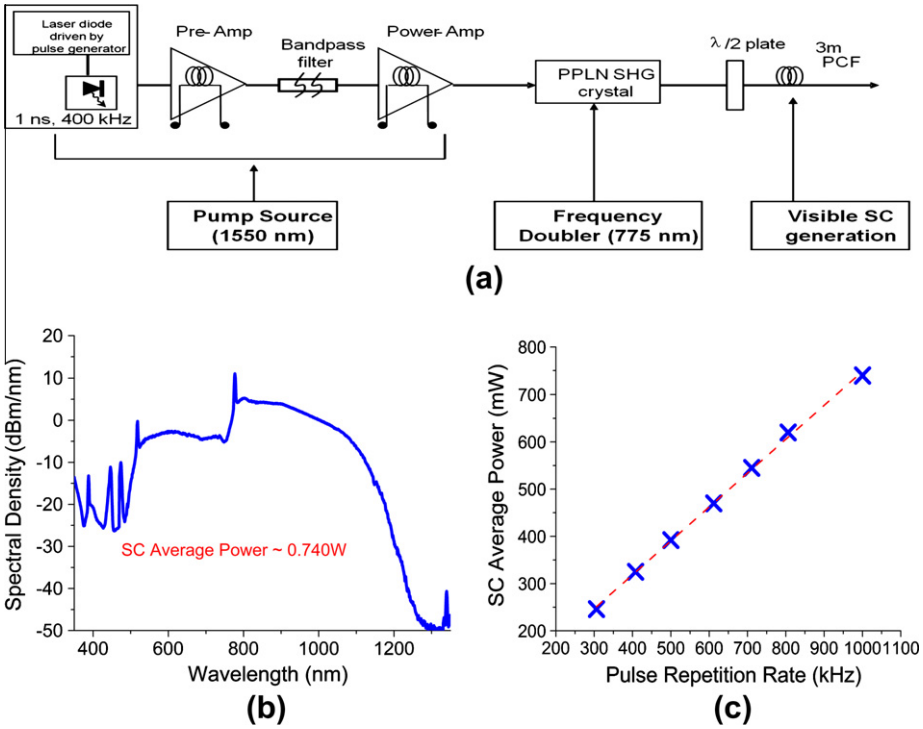

Fig. 10. (a) Experimental setup for visible SC generation. (b) Visible SC spectrum output. (c) SC average power scaling with repetition rate [29].

generation mechanisms responsible for each side. The long wavelength side of the spectrum experiences additional gain due to stimulated Raman scattering, which transfers power from the shorter to longer wavelengths. On the other hand, wavelengths below the pump are generated primarily by phase matched four wave mixing. The smooth nature of the continuum can be attributed to the ensemble average of the spectra produced by the multiple solitons within the 2 ns pulse envelope.

We also perform measurements to maximize the second harmonic generation efficiency. Since the PPLN crystal has a limited doubling bandwidth of ~1 nm, spectral broadening in the amplifier reduces the SHG efficiency. To reduce the nonlinearity, we minimize the length of the SMF fiber to ~0.5 m. Next, we vary the input peak power to obtain the maximum SHG efficiency of ~70% at 1 kW peak input power. The transmission loss through the crystal at low power is measured to be ~30%.

Power scalability of this system is also demonstrated. Since the nonlinear phenomena responsible for SC generation are peak power dependent, the average power in the continuum is scaled up by increasing the repetition rate of the seed laser and the pump diode power, while keeping the 1.5 μm peak power (and, hence, the spectral shape) constant around 1 kW. Fig. 10c shows an approximately linear increase in the SC average power from 250 mW to 740 mW with an increase in the repetition rate from 300 kHz to 1 MHz. The average power could be scaled up further by using a larger core gain fiber (to reduce the amplifier nonlinearity) and by increasing the amplifier pump power.

Thus, we have demonstrated SC systems covering the wavelength region from the mid-IR to the visible wavelengths utilizing the framework depicted in fig 1. An advantage of the MI initiated SC architecture, as we see in the SC systems described in this section, is the scalability of the SC average power by simply increasing the repetition rate and the corresponding amplifier pump powers. By adjusting the pulse width, repetition rate and the pump powers, this architecture allows the average power to be scaled up while keeping the peak power, and, hence, the SC spectrum approximately constant.

4. Simulations

In this section, we present simulations to better understand some of the experimental results in Section 3. In particular, we look at three experimental results. First, we verify the validity of the simulator by comparing the experimental results with simulations for the SC output from the TDFA based system in Section 3.1.3. Next, we use simulations to better understand the dependence of the final SC spectrum on the first stage SC, that serves as the input seed for the TDFA amplifier in Section 3.1.3. Finally, we present simulations to compare the SC spectrum for the EYFA based system in Section 3.1.2 with the SC spectrum from the TDFA based system shown in Section 3.1.3.

In the fiber the complex envelope $A(z,\tau)$ of a pulse under the slowly varying approximation satisfies the generalized nonlinear Schrödinger equation (GNLSE) given by [53].

$$\frac{\partial A}{\partial z} = (\hat{D} + \hat{N})A$$

$$\hat{D} = \sum_{k\geqslant 2} \frac{i^{k+1}}{k!}\beta_k \frac{\partial^k}{\partial \tau^k} - \frac{\alpha}{2}$$

with

$$\hat{N} = i\gamma\left(1 + \frac{i}{\omega_0}\frac{\partial}{\partial \tau}\right)\int_{-\infty}^{+\infty}[(1-f_R)\delta(\tau') + f_R h_R(\tau')] \times |A(z,\tau-\tau')|^2 d\tau'$$

where the pulse moves along z in the retarded time frame $\tau = t - z/v_g$ with the center angular frequency, ω_0. The terms in the differential operator $\hat{D}$ accounts for the dispersion as well as the loss (α) of the fiber. The refractive index versus wavelength data is estimated from the Sellmeier equation using parameters provided by the manufacturers or from the literature. The corresponding dispersion versus wavelength data is then calculated and used in our simulations. The terms in the operator $\hat{N}$ result from nonlinear interactions, which describe SPM, self steepening, and SRS effects. In particular, the effective nonlinearity is defined as $\gamma = n_2\omega_0/cA_{eff}$ where n_2 and A_{eff} are the nonlinear refractive index and the effective mode area in the fiber, respectively. In addition, $h_R(t)$ represents the Raman response function, and f_R is the fractional contribution of the Raman response to the nonlinear polarization. The GNLSE described above is solved by a modified adaptive split-step Fourier method with the initial pulse shape as the known boundary value. Further details for the input parameter values such as the nonlinear parameters and Raman gain are given in [33,51]. Splice losses as observed experimentally are also included in the simulation model.

To verify the validity of the simulator, we compare the experiment results and simulations for the TDFA based system presented in Section 3.1.3. For the simulations presented in this paper, we use super-Gaussian pulses with ~80 ps FWHM and center wavelength at 1553 nm to satisfy the quasi-CW conditions and to keep the computation times reasonable. Fig. 11 shows the comparison between experiments and simulations of the output spectrum from 25 m SMF with ~2.5 kW peak input power at 1553 nm and the corresponding second stage SC from the output of the ZBLAN fiber. The TDFA stage is simulated with ~12 dB of gain, as is observed in the experiments. The single run simulation shows several spectral features due to the smaller pulse width used in the

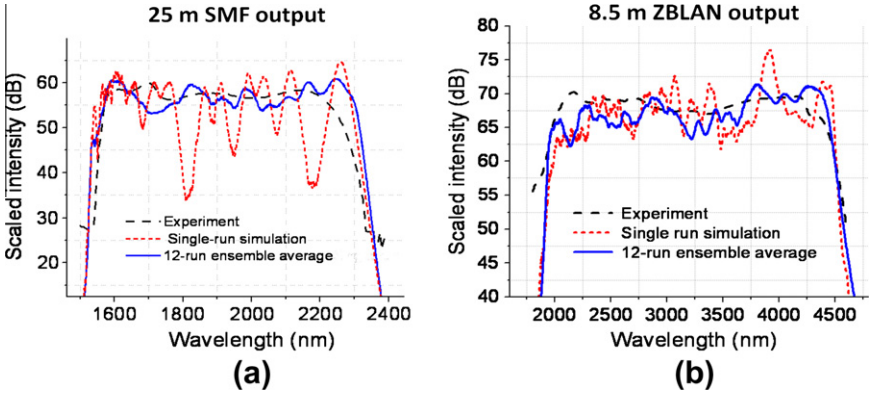

Fig. 11. Comparison of simulation versus experimental results for the TDFA based SC system. (a) Output from the first stage SC consisting of ~25 m SMF. (b) Output from ~8.5 m length of ZBLAN fiber [51].

experiments and with the measurements settings used, the experimental results are in reality a average of over 150,000 instances of the 1.55 μm input pulse. The ensemble average of 12 simulations with different noise seeds show a trend towards the reduction in fluctuations in the spectrum as is observed in the experiments. As expected, the outputs of the simulations from different runs show some variation due to the evolution of the spectrum from background noise. The simulations show a reasonable agreement with the experimental data. For the fused silica case, the simulation output shows a slightly longer wavelength edge compared to the experimental data, due to the larger mode profile dispersion in SMF, due to an NA of 0.13. For the ZBLAN SC, the simulations show a higher depletion of the first stage SC pump at ~2 μm, due to the cutoff wavelength of the ZBLAN fiber at ~2.75 μm, which suggests that some of the coupled 2 μm light into the ZBLAN fiber may not be in the fundamental mode, and hence would not contribute to the spectral broadening process due to the lower field intensity of the higher order modes, and would remain undepleted at the end of the ZBLAN output.

For the TDFA based SC system in Section 3.1.3, one would expect the second stage ZBLAN SC to extend further in wavelength as the peak power of the 1.55 μm pulses used in the first stage SC generation is increased. However, the experimental results in Fig. 12 show that lower (1.5 kW) peak power, 1.55 μm pulses used in the first stage SC generate a longer extending second stage SC in ZBLAN compared to when higher (2.5 kW) peak power, 1.55 μm pulses are used in the first stage SC. In addition, the second stage ZBLAN SC generation efficiency is experimentally observed to be lower for the 1.5 kW case compared to the 2.5 kW case. To better understand these counterintuitive phenomena, we perform simulations (single run) to show the spectral output of the second stage ZBLAN SC and the temporal profile of the input to the second stage ZBLAN SC. The wavelength associated with the time domain pulses at the input of the ZBLAN consist mostly of the pump wavelength, ~1.55 μm for the EYFA systems and ~2 μm for TDFA systems. Simulation results are seen to match the experimental results, whereby, lower (1.5 kW) peak power, 1.55 μm pulses used for the first stage SC generation leads to a longer extension of the ZBLAN output spectrum, compared to when 2.5 kW peak power pulses are used. The time domain simulations in Fig. 12 show that the 2.5 kW, 1.55 μm pulse peak power used in the first stage SC generates, at the output of the TDFA, a larger number of relatively low peak power ~2 μm pulses. In comparison, for the 1.5 kW peak power, 1.55 μm pulse case, we see a smaller number of ~2 μm pulses with higher peak power evolve in the TDFA. Thus, the time domain simulation results show that the TDFA output pulses for the 1.5 kW case are fewer and has a higher peak power than the 2.5 kW case and will therefore, generate a longer wavelength extending SC in ZBLAN fibers. Also, since the duty cycle in the 2.5 kW case is larger due to the presence of larger number of ~2 μm pulses, the ASE generated can be expected to be lower, leading to higher pump depletion and, thus, a higher SC generation efficiency in the ZBLAN fiber.

Finally, simulations are also done to compare the output from ZBLAN fibers in the EYFA (Fig. 5b) and the TDFA (Fig. 6b) based systems. An 8.5 m length of ZBLAN is used for the simulations in both systems so that the material loss properties would be kept identical. For the EYFA simulations, 20 kW of peak power pulse at 1.55 μm is input into a ~1 m length of SMF, and the output is coupled into 8.5 m length of ZBLAN fiber after accounting for the mechanical splice loss. Fig. 13a compares the single run output spectrum in the two cases and shows that the SC spectrum extends

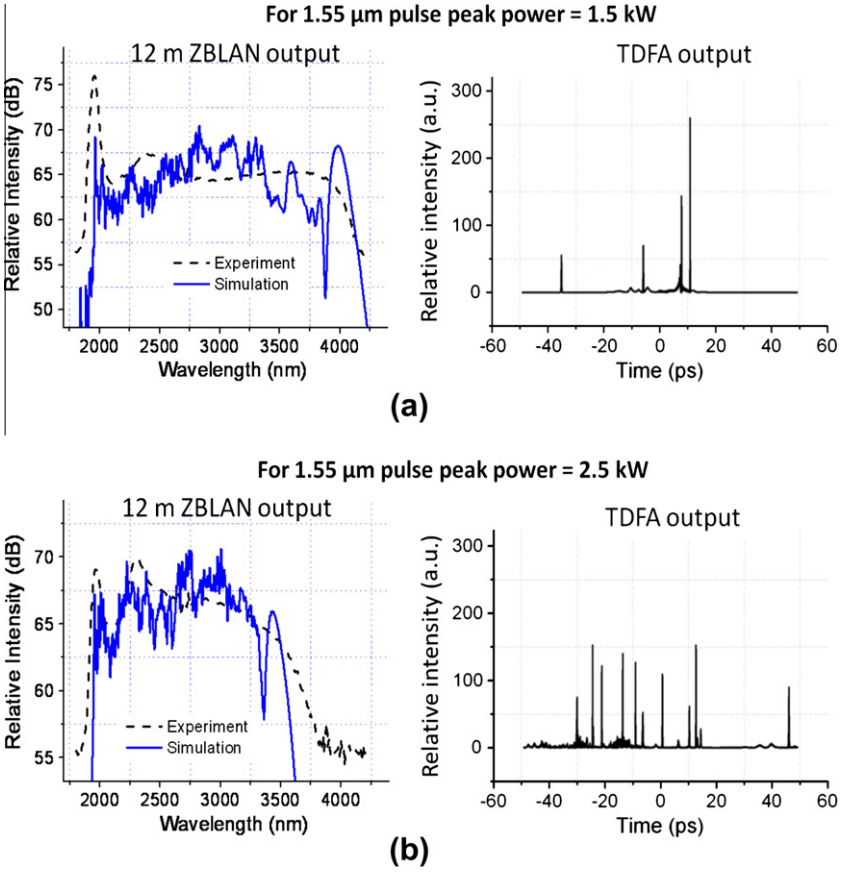

Fig. 12. Simulations results showing the dependence of 1.55 μm input peak power used for first stage SC on the ZBLAN output. Spectral and temporal simulations for ZBLAN and TDFA output respectively, with (a) 1.5 kW input peak power and (b) 2.5 kW input peak power [51].

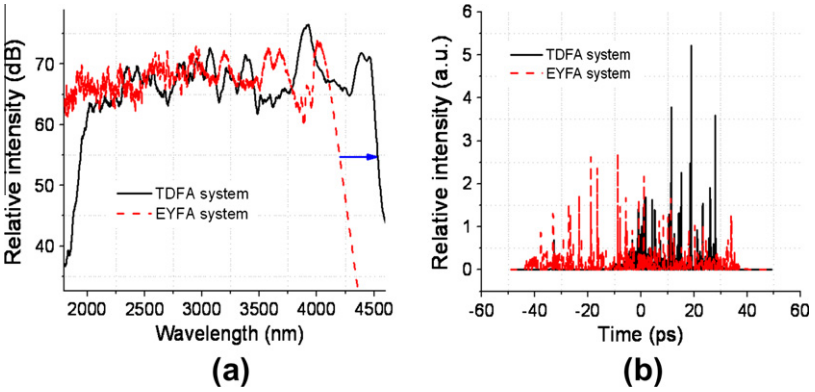

Fig. 13. Simulation results comparing the (a) output spectrum of 8.5 m length of ZBLAN fiber for the TDFA and the EYFA based systems and (b) pulse profile comparison at the input of the ZBLAN fiber in the two systems [51].

~330 nm further in the TDFA system compared to the EYFA system and is close to the ~270 nm as observed in the experiments. Fig. 13b shows the corresponding input pulse profile to the ZBLAN fibers in the two cases. In the EYFA system case, the simulations suggest that the MI-initiated pulse breakup process in the 1 m length of SMF after the EYFA amplifier stage gives rise to high peak power pulses responsible for long wavelength generation in ZBLAN fiber. In comparison, for the TDFA system, simulations show that the amplification of the wavelength shifted components in a 25 m length of SMF around 2 μm yields a pulse profile with higher peak powers, which would explain the longer extending spectrum in the same length of ZBLAN fiber compared to the EYFA-based mid-IR SC laser.

5. Applications of fiber SC sources

The broad wavelength bandwidth and high average power of all-fiber SC lasers are key enablers for a variety of applications in several industries. For example, in the defense and security industry, the mid-IR SC spectrum can be used to emulate black body radiation of hot objects. The mid-IR SC also overlaps with the vibrational and rotational resonances of many solids and we utilize this feature to develop a mid-IR SC system for standoff detection of solid targets, such as explosives and other chemicals. In the health care industry, the mid-IR SC laser can be a useful tool to perform diagnostics and therapeutics. For example, we demonstrate the use of a mid-IR SC laser to perform atherosclerotic plaque detection and to cause preferential damage to lipids, which are a main component of such plaques. The plaque detection and preferential damage is possible since the absorption of carbon–hydrogen bonds that are the main building blocks of lipids fall within this wavelength region. In addition to the broad wavelength coverage and the high average power, the ability to easily focus and collimate the SC light enables measurements of flat as well as curved surfaces over large working distances, and is particularly attractive for metrology applications. For example, we use the spectral dependence of reflected light from a near-IR SC light source to perform surface roughness measurements of flat and curved machined metal parts with a working distance of >0.8 m from sample to detector. The broad bandwidth also allows precise depth resolution measurements, as is demonstrated in a high resolution line scan interferometer, using the visible SC source.

5.1. Stand-off detection of solid targets

We demonstrate the use a mid-IR SC laser to detect solid targets at a stand-off distance of 5 m using diffuse-reflection spectroscopy [2]. The SC source is used to obtain the reflection spectra of a wide range of samples including explosives, fertilizers and paint coatings. We observe unique spectral fingerprints in the near and mid-IR wavelength regions of the reflection spectrum and develop a correlation function based algorithm to distinguish between the samples. The demonstrated SC light source has excellent beam quality due to the single mode fiber output, covers multiple atmospheric transmission windows and is all-fiber integrated with no moving parts or free space optics. Thus, it is well suited for spectroscopy applications in a wide range of fields such as defense, homeland security, remote sensing and geology.

Diffusion reflection spectroscopy is a widely used technique for both qualitative and quantitative analysis of IR active samples. Some of the common techniques used, include the use of a conventional FTIR instrument fitted with an attenuated total or diffuse reflectance setup [59], remote Raman spectroscopy and laser induced breakdown spectroscopy (LIBS) [60]. In the case of FTIR measurements, the sample is confined to the sample chamber, thus limiting its use to offline measurements in a laboratory setting. While Raman spectroscopy offers excellent overall selectivity, some samples are difficult to analyze due to the fluorescence caused by the intense pump beam. In addition, there is a need for extremely sensitive detection with large collection optics due to the inherent weak nature of the Raman effect. However, improved sensitivity has been reported by the use of resonance Raman spectroscopy [61] and Coherent anti-stokes Raman spectroscopy [62]. In LIBS, the high beam intensity required for the breakdown of the sample limits the spot size on the sample to a few millimeters and may cause thermal degradation of the sample. In comparison, our technique uses a spatially coherent beam from the mid-IR SC laser to measure the diffuse reflection spectra of solid samples. The 3000 nm wide output spectrum covers multiple fundamental and overtone molecular vibration absorption bands, and allows the measurement of a wide range of samples. In addition, the high output power and single mode beam quality enable simple stand-off measurements. The reflection spectra obtained using our technique show good agreement with those reported in the literature using conventional methods such as the FTIR or a spectrophotometer.

The SC source used for this experiment is described in Section 3.1.2. Fig. 14 shows the experimental setup used in the diffusion reflectance spectroscopy setup. The SC output is first collimated using a parabolic mirror and is incident on a sample kept at ~5 m from the collimating mirror. The beam is incident normally on the sample, but detected at a reflection angle of ~2.3°. A 12 cm diameter concave mirror with a 75 cm focal length is used to collect a fraction of the reflected light from the sample

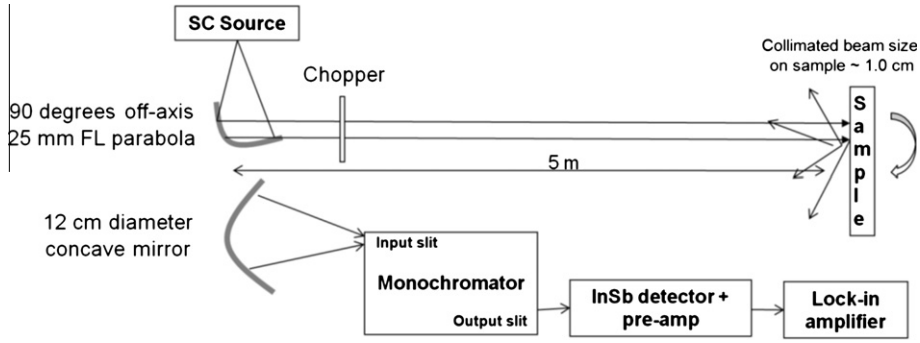

Fig. 14. Experimental setup for SC based stand-off diffuse reflection spectroscopy [2].

and focus it to the input slit of the monochromator. The output slit is set to 2 mm corresponding to a spectral resolution of 10.8 nm and the light is detected using a liquid nitrogen cooled indium antimonide detector. The chopper frequency is 400 Hz, and the lock-in time constant is set to 100 ms, corresponding to a noise bandwidth of ~1 Hz. The scan is performed across the wavelength region from 1.2 to 4.2 μm. Appropriate wavelength filters were used to avoid contribution from the higher wavelength orders from the grating. The reflection spectrum of a given sample is normalized to the reflectance form Infragold, an electrochemically plated diffuse gold metallic coating with a nearly ideal Lambertian scattering profile that is kept at the same distance as the sample. A 45° fold mirror was used for samples such as powders that could not be oriented in the vertical plane normal to the collimated SC beam. The percentage sample reflectance is obtained by dividing the sample scan by the Infragold reference scan, followed by smoothening of the reflectance curve using a 5 point Savitzky–Golay filter [63]. For certain samples, the reflectance curve is transformed to a pseudo-absorbance curve using the transformation $A = \log(1/R)$ for better visualization of the features of interest.

For the spectra measurements, our sample consists of 4–8% of explosives, such as TNT, RDX, PETN and potassium nitrate on a fused silica substrate. The absorbance spectra measured using the SC laser is shown in fig 15. In each case, the spectral features are characteristic of the stretching vibrations specific to the molecular make up of the samples. The strongest absorption features in TNT, RDX, and PETN are in the 3200–2500 nm band, and arise due to the fundamental aromatic and aliphatic C–H stretch. The spectral features around 3600 nm in potassium nitrate are due to the first overtone of the N–O asymmetric stretch. The common broad feature at 2720 nm in all four samples is due to the O–H stretch from absorbed water in the fused silica host. In order to verify the validity of our measurement system, we also compare the spectral features with reported measurements in the literature and see them to be in good agreement [64–66].

SNR calculations are also performed to determine the smallest relative percentage change in sample reflectivity that can be measured at a given stand-off distance as a function of the lock-in time constant used for the measurements. Fig. 16 shows the variation in SNR versus the sample stand-off distance. We see that at distances below 10 m, our measurements are limited by SC fluctuation noise. However, at longer distances SNR begins to be detector noise limited. The system sensitivity, a function of SNR, can be improved by scaling up the SC power by using higher repetition rates and pump powers. Using a detector with a smaller area will also help to improve sensitivity, since the noise equivalent power is proportional to the detector area. SNR can also be improved by averaging the spectra measurements. Using a detector array, rather than a

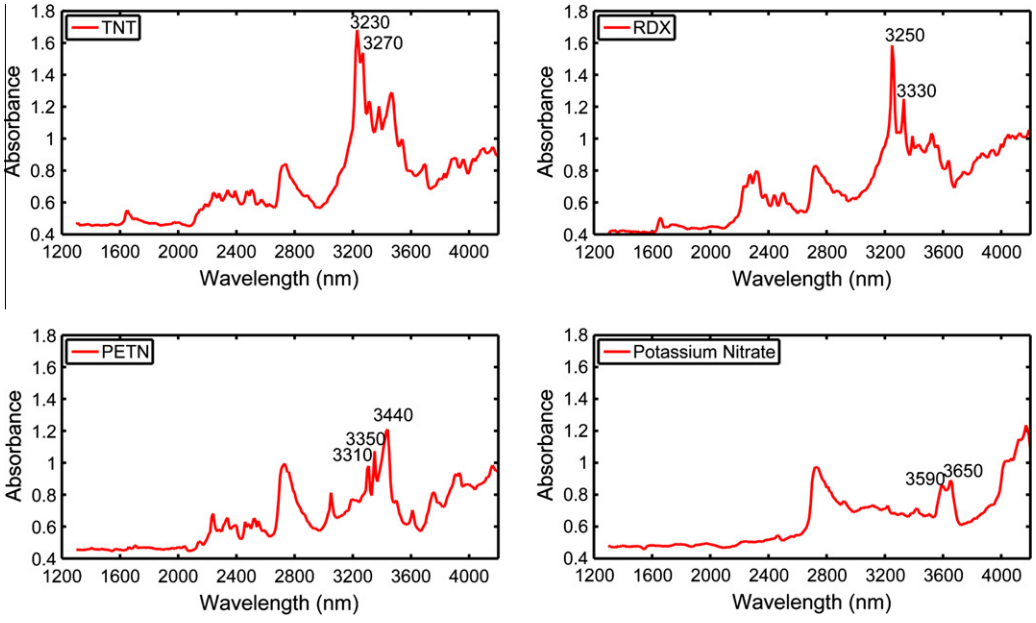

Fig. 15. Mid-IR SC Absorbance spectra of explosives – TNT, RDX, PETN, potassium nitrate [2].

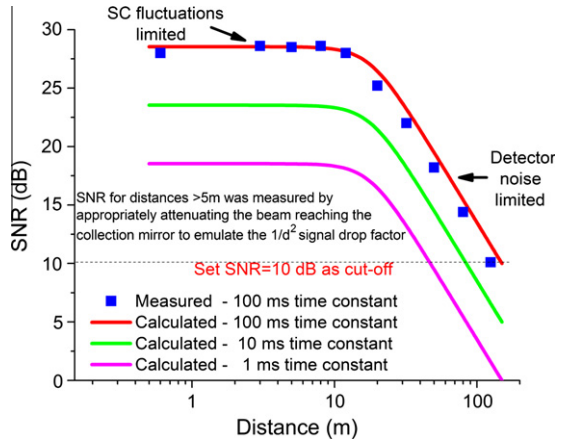

Fig. 16. Variation in SNR versus the sample stand-off distance. At small distances, the noise is dominated by the SC fluctuations, while at large distances the detector noise is dominant [2].

grating spectrometer will allow faster measurements and averaging to be done without adding on to the measurement time.

Thus, we have measured the reflection spectra of various solid samples at a stand-off distance of 5 m, using a mid-IR SC light source with 3.9 W average output power and spectrum extending from 0.8 to 4.2 μm. For each sample, we observed unique spectral features in the reflection spectrum, attributed to the fundamental and overtone vibrational frequencies of the various molecular bonds in the sample structure. We also calculated and verified experimentally, the variation of SNR with distance. For a time constant of 100 ms corresponding to ~1 Hz noise bandwidth, we obtained a SNR of ~625 at distances <10 m. Assuming a minimum detectable SNR of ~10, the maximum standoff distance with the current SC output power and integration time is determined to be ~150 m.

5.2. Atherosclerotic plaque detection and preferential damage of lipids

As an application of mid-IR SC lasers for biophotonics, we performed spectroscopy and demonstrate preferential damage of the constituents of vulnerable plaque in the artery [67]. Heart attack is caused by the clot formation in coronary arteries due to the rupture of vulnerable atherosclerotic plaque (AP) [68]. In the AP of an affected artery, smooth muscle cells migrate to form a fibrous cap that overlays atherogenic matter including lipids, macrophages and foam cells [68]. We observe distinct spectral signatures of the constituents of AP in the 3.2–3.6 μm wavelength window. In the mid-IR region between 2.6 and 3.8 μm, lipids and proteins have fundamental absorptions that lie at different wavelengths. Therefore, we exploit the difference in spectral features for potential diagnostics for ailments associated with lipid rich tissues. Differential damage of lipids without damaging the protein-rich blood vessel wall of the artery is possible because proteins show primary light absorption in at 2.8–3.2 μm due to N–H and O–H bonds, while lipids exhibit absorptions in 3.2–3.6 μm associated with C–H stretching vibrations. We use absorption spectroscopy to identify or differentiate the constituents of the normal artery and atherosclerotic plaque, including adipose tissue, macrophages and foam cells. In addition, by using light in 3.2–3.6 μm that targets the lipid absorption lines, we demonstrate differential damage to lipid-rich samples such as adipose tissue without damaging the normal aorta.

The fiber based SC laser provides a new platform for spectroscopy measurements and tissue ablations in the mid-IR. Conventionally, thermal lamps, optical parametric amplifiers [69], quantum cascade lasers [3], broadband femtosecond lasers [70] and synchrotron lasers [71] have been used as light sources for mid-IR spectroscopy applications. However, SC based absorption spectroscopy experiments in the mid-IR where the fundamental molecular vibrational modes reside have not yet been reported. Single wavelength selective ablation has also been performed in the 5.75 um to 6.1 μm region for ablation of cholesterol esters using a free electron laser [72]. Differential damage of lipid rich tissues has also been reported using lipid absorption bands around 1210 nm [4] and 1720 nm [4,73]. In comparison, our all fiber integrated mid-IR SC laser has been packaged into a 2U rack unit (19 in. in width/21 in. in depth/4 in. in height), has no moving parts, generates the entire spectrum simultaneously in the single spatial mode, operates at room temperature and could potentially be used in the clinical environment for practical medical use.

The SC source used for this experiment is described in Section 3.1.1. Fig. 17 shows the experimental setup used and consists of three main parts: the SC laser, mid-IR spectroscopy and the laser ablation. It should be noted that although the SC laser has been demonstrated with up to 10.5 W average output power, the spectroscopy measurements and laser damage are conducted with only a few of the pump laser diodes on, and ~1.5 W SC output power. For the absorption spectroscopy measurements, the SC is first collimated using a parabolic mirror and then split into one signal arm that passes through the sample under test and one reference arm. The two arms are modulated by choppers at different frequencies and the recombined light is coupled into a grating based monochromator, where the signal is collected by a liquid nitrogen cooled indium antimonide detector. For the preferential damage setup, shown in Fig. 17 b, the SC light for targeting lipids is chosen by filtering out light below 3.2 μm using a long pass filter. The light is then focused by a 25.4 mm calcium fluoride lens to a spot size of ~3 mm on to the sample. The spectroscopy and the selective ablation are performed in vitro on the tissue and cultured cells respectively.

Mid-IR SC absorption spectra of the components of normal artery, which includes endothelial cells and smooth muscle cells is illustrated in Fig. 18a and b. The broad absorption feature from 2.8 to 3.2 μm with a peak at ~3.05 μm is observed and can be attributed to the vibrational bands of O–H stretching in the hydroxyl group and N–H stretching present in the protein amino acids [71,74]. The spectra for the constituents of atherosclerotic plaque, including macrophages, adipose tissue, and foam cells are also illustrated in Fig. 18. In the lipid-rich samples such as the adipose tissue and foam cells, we can distinguish the absorption lines in the 3.2–3.6 μm window, for example, the C–H stretching vibration at ~3.33 μm, CH_3 stretching vibration at ~3.39 μm, and CH_2 stretching vibration at ~3.42 μm and ~3.510 μm [74]. It is worth noting that while the macrophages exhibit a similar absorption spectrum as compared to the normal artery cells, prominent spectral characters between ~3.2 and 3.6 μm with two absorption peaks at ~3.42 and 3.51 μm are observed in the macrophages-transformed foam cells and adipose tissue absorption spectra, revealing the pathological relationship between these two cell types, i.e. active macrophages engulfing lipid-rich substance to become foam cells.

Preferential damage takes advantage of the differential absorption of different tissues where by the targeted tissue is preferentially heated to a temperature lethal to cells by laser radiation within the corresponding signature absorption band. We hypothesize that by using laser radiation targeting the lipid absorption band from 3.2 to 3.6 μm, we can heat adipose tissue to a damage threshold faster than the artery tissue. Preferential heating (or thermal modification) of adipose tissue without damaging artery tissue, is observed under light microscopy (Fig. 19) with an SC laser fluence starting as low as ~15 mJ/mm^2, while no damage was observed to the artery up to ~100 mJ/mm^2. The beam diameter used

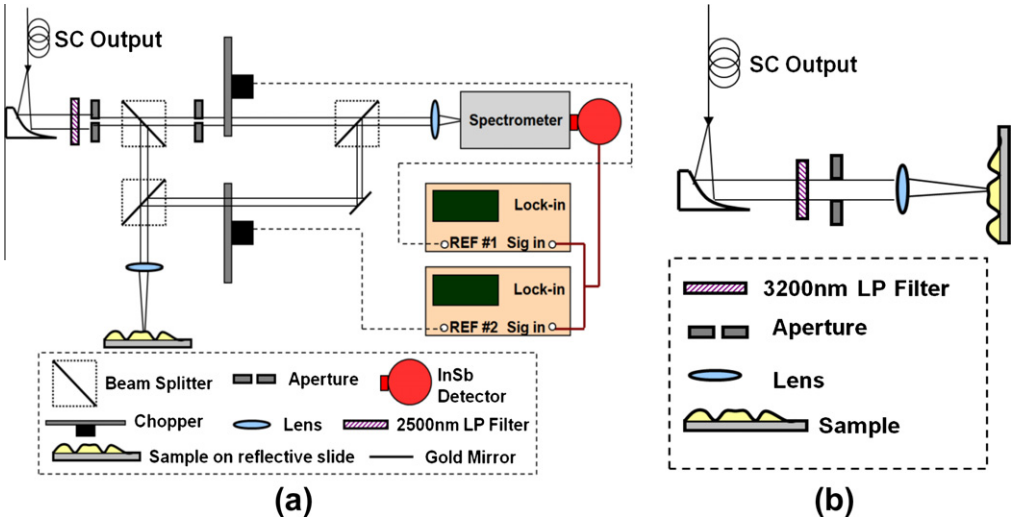

Fig. 17. (a) Reflection–absorption spectra measurement setup, (b) preferential laser ablation setup [67].

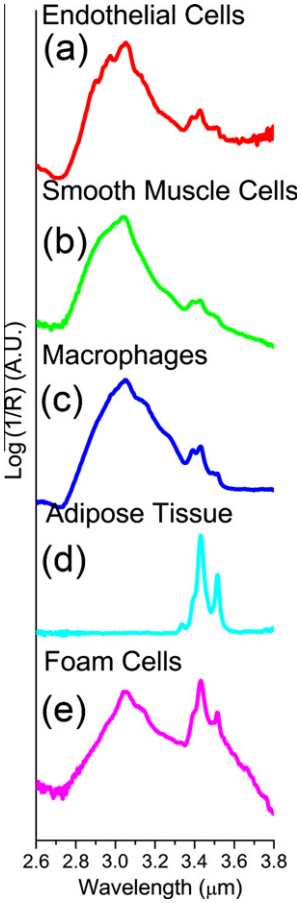

Fig. 18. Mid-IR SC laser based reflection–absorption spectra of normal artery compositions: (a) endothelial cells, (b) smooth muscle cells; and atherosclerotic plaque constituents, (c) macrophages, (d) adipose tissue, and (e) foam cells [67].

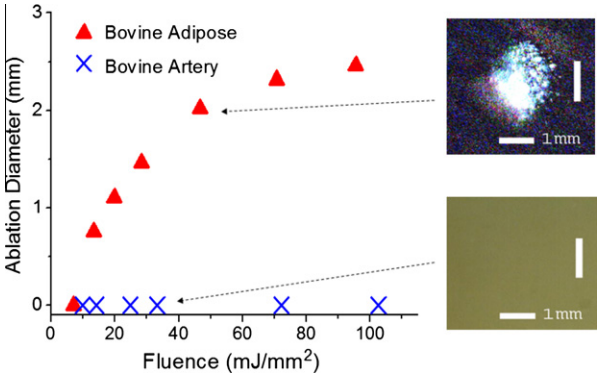

Fig. 19. Power dependence of the damage diameter in adipose tissue and bovine artery, right, images showing the difference before and after laser damage at ~40 J/mm^2 [67].

is ~3 mm and the exposure time used is 5 s. Fig. 19 also shows the image subtraction of before and after laser treatments to identify damage of the adipose and artery tissues. For the adipose tissue, the damaged region is in bright color while the unaffected region is dark color. Histochemistry study was also performed to better understand the biological integrity and damage to the artery and we observed that while laser induced damage can be observed at a laser fluence of ~102 mJ/mm^2, no such effects are present at ~33 mJ/mm^2 and very subtle wounds exist at ~72 mJ/mm^2.

Thus, mid-IR absorption spectra of normal artery and AP compositions are measured using an all-fiber mid-IR SC Laser. Distinctive spectral signatures in the 3.2–3.6 μm range associated with fatty acids and cholesterol esters absorption are present in the components of AP, including foam cells and adipose tissues. On the other hand, endothelial cells, smooth muscle cells and macrophages have a more dominant feature at 2.8–3.2 μm, corresponding to protein and water absorption. Preferential damage of the lipid-rich material has been demonstrated using the mid-IR SC laser to target the 3.2–3.6 μm fatty acids and cholesterol esters absorption band under laser fluence ranging from ~15 to 40 mJ/mm^2. The absorption spectra acquired using our SC laser is consistent with the measurements conducted using either a traditional lamp or synchrotron laser based FTIR measurement system [71,75,76]. The demonstrated differential damage of adipose tissues versus healthy artery also suggests potential therapeutic method using the mid-IR SC laser. Therefore, with the dual capability of locating atherosclerotic plaque and differential damage, the mid-IR SC laser could potentially be used to diagnose atherosclerosis disease. Treatment might be accomplished in a catheter-based, minimally invasive procedure that could be an add-on to the angiogram (i.e. use the guide wire already in place to insert the mid-IR catheter.

5.3. Surface roughness measurements

As an application of SC lasers in the metrology field, we demonstrate a system using a NIR fiber SC laser for performing high accuracy, non-contact RMS roughness measurements of flat and curved machined metal parts in the industrially relevant range of ~0.05–0.35 μm [77]. The system uses an SC laser that extends from ~1 to 2.5 μm with ~25 mW (similar to the setup in [33]) of average power to measure the intensity of specular reflection versus wavelength from a sample of interest, at relatively long (~1 m) standoff distances and has the potential to be used in high speed, in-line manufacturing applications.

Parts that are finished using lapping or polishing commonly have surface roughness values in the 0.05–0.4 μm range [78]. Two important examples of such polished parts are crankshaft and camshaft journals for internal combustion engines. The surface roughness of crankshaft and camshaft journals and bearings is one of the factors that controls friction and influences the performance and fuel economy of engines [79,80]. Improvements in the tribological performance of engines can provide a variety of benefits such as reduced fuel and oil consumption, increased power output, reduction in harmful emissions, and improved durability and reliability of engines [80]. Conventional techniques for roughness measurements include the mechanical stylus and white light interferometry. However, most of these techniques are limited by the working distance, sample curvature, etc., and are not very practical for in-line measurements. On the other hand, roughness measurement using the SC laser has advantages that include a constant area of illumination/data collection and the potential for high measurement speed since the sample and the detector are all in a fixed position. The SC laser also provides the ability to collimate and focus the light easily, which enables the measurements of curved surfaces such as the cylindrical crankshaft journals used in our experiments.

The system makes roughness measurements utilizing the Beckmann (BK) scattering model [81], which suggests that the normalized specularly reflected light (the sample reflectance is normalized to the reflectance from a smooth sample of the same material) from a surface, at a fixed angle of incidence, is a function of the wavelength of the incident light and the surface roughness. For example, if the wavelength is of the same order as the surface features, most of the light is going to be scattered away from the specular direction. The same surface begins to look smoother as the wavelength increases and the light reflected in the specular direction will increase with the wavelength. Thus, by looking at the wavelength signature, in particular, the slope of the reflectance versus wavelength of the reflected SC light, we are able to extract the roughness parameter for the surface. It is therefore important to choose correct wavelength region for a given range of roughness values.

The SC source used for this experiment is similar to the near-IR SC system described in Section 3.2. In this case, the SC is generated entirely in SMF, extends from ~1.0 to 2.5 μm and provides the necessary bandwidth required for the roughness measurements.

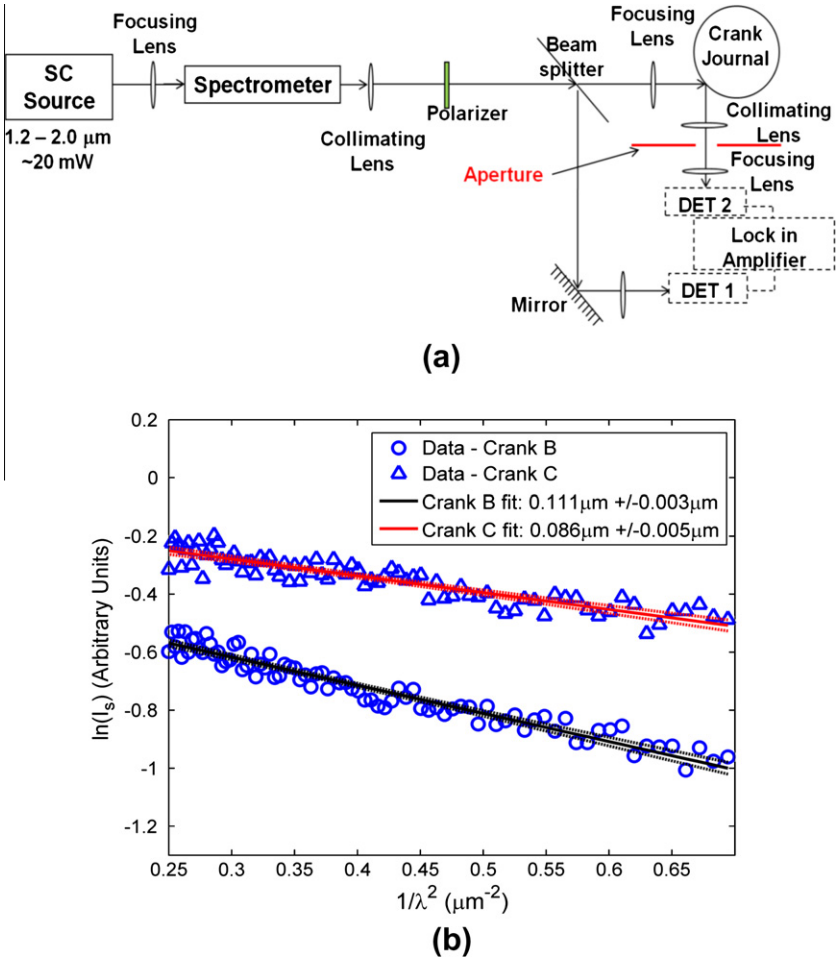

Fig. 20. (a) Experimental setup for the surface roughness measurement system. (b) Normalized reflectance spectrum and extracted roughness values for Cranks B and C, dotted lines show the confidence limits [77].

Fig. 20a shows the layout of the surface roughness measurement system. The SC light passes through the spectrometer and is incident on the sample at a fixed angle of incidence. The light is collimated (~2 mm beam diameter) for flat samples and focused (350 μm beam diameter) for the curved samples. A dual beam detection approach is used to minimize any effects of the source fluctuations, where by the light is split into two arms: the sample and the reference arms. The reference arm consists of a gold mirror and the reflected light is captured by an InGaAs detector, Det 1. The specular component from the sample is captured by the InGaAs detector, Det 2. A combination of apertures is used to filter out any non-specular components of the reflected light from the sample. The monochromator slit settings are 100 μm and yield a nominal spectral resolution of ~0.5 nm. The lock-in time constant is 300 ms. We collected ~80 wavelength samples evenly spaced between 1.2 and 2.0 μm and a typical measurement time/spot is ~120 s. The measurements are performed up to only 2 μm due to the detector cut off of about 2.2 μm.

Our system is capable of performing roughness measurements of flat as well as curved surface. We measure two flat samples and five cylindrical crankshaft journals labeled Crank A–E with varying surface finishes. As an example, Fig. 20b shows the normalized reflectance spectrum both for Crank B and Crank C. The simulation fits, using the BK model and the corresponding extracted roughness values and 95% confidence limits (dotted lines) are shown in Fig. 20b. The slope difference between the two roughness values is also evident in Fig. 20b, where larger slope corresponds to a higher roughness value. Table 2 shows the roughness values for our samples obtained using the SC laser with other standard techniques such as the mechanical stylus based profilometer and the while light interferometer. For each sample, the roughness measurements were performed at three random points and the average and standard deviation are noted in the table. We were not able to measure Crank E using the white light interferometer, since the roughness value is below the measurement range using available settings. The roughness value of crank D is above the measurement range of our system.

An added advantage of performing roughness measurements in the near-IR is the lack of requirements for a reference of the same material as the sample. This can be explained by the fairly flat reflectance signature of metals, like gold and aluminum, in the near infrared wavelengths and beyond. The wavelength shape of the normalized reflectance in the Infrared is then mostly due to the surface features and is more or less independent of the metal property of the reference itself. In principle, the roughness range of interest for crank journals and metal parts can be measured using scattering in the visible region; however, different metals have widely varying reflectance signatures in the visible region. This makes it mandatory to have a reference of the same material or to correct for the wavelength signature of the reference for measurements done in the visible region. Our measurements are performed using a gold mirror as a reference and are seen to be in good agreement with values obtained using other standard techniques, as shown in Table 2.

Table 2
Comparison of RMS roughness values measured using different techniques.

Sample	Supercontinuum (μm)	White light interferometer (μm)	Stylus (m)
Flat A	0.148 (0.005)	0.146 (0.004)	0.136 (0.005)
Flat B	0.324 (0.018)	0.330 (0.026)	0.326 (0.020)
Crank A	0.081 (0.004)	0.091 (0.002)	0.088 (0.006)
Crank B	0.109 (0.011)	0.111 (0.015)	0.115 (0.014)
Crank C	0.087 (0.004)	0.093 (0.008)	0.087 (0.010)
Crank D	NA	0.774 (0.045)	0.757 (0.039)
Crank E	0.049 (0.003)	NA	0.047 (0.005)

Thus, we have demonstrated a non-contact RMS surface roughness measurement system capable of measuring roughness values in the range of ~0.05–0.35 μm, from the slope of the wavelength dependence of reflected light, using a super-continuum laser, from 1.2 to 2 μm. The roughness values obtained using the SC laser are compared with those from a stylus based profilometer and a white light interferometer and shown to be in good agreement. The SC laser provides the ability to collimate and focus the light, which is critical for roughness measurements of curved surfaces using this technique. We have successfully demonstrated the broadband super-continuum laser as a key enabler for wavelength dependent roughness measurements of flat and curved surfaces with large working distances of greater than 0.8 m from the sample to the detector. The roughness measurement range and working distance can both be increased by SC laser systems being developed with longer wavelength bandwidths and higher power. The combination of sub-micron roughness measurements at a large working distance along with the capability to measure both flat and curved surfaces, like crankshaft journals, makes the system an attractive tool for inline inspection in the industry.

5.4. High resolution line scan interferometer

As a final example, we demonstrate a high resolution line scan interferometer comprising of a 1553 nm frequency doubled visible SC laser with 125 nm axial resolution and 15 μm lateral resolution for 3D inspection of curved surfaces [82]. While the broad bandwidth (600–700 nm) of the SC source is responsible for the high axial resolution, it is the high average output power of ~5 mW that enables the measurement of curved surfaces that reflect light away from the receiver. We demonstrate the interferometer system to detect shape defects and measure the height of solder balls in solder ball grid arrays.

Reduction in size of semiconductor devices has lead to an increased density of chips on a wafer. As a result, solder ball grid arrays are being increasingly used to flip-chip bond with an external circuit. The reliability of electrical contacts depend on the shape and size of solder balls deposited on the chip, and thus their inspection is an important aspect of quality control [83]. Current 2D inspection techniques use machine vision that can measure the ball diameter and location, but provide no information on the height. 3D techniques such as laser triangulation and confocal microscopy have been used to measure the ball height but provide no shape information [83].

The SC source used for this experiment is described in Section 3.3. The SC extends from 0.5 to 1.2 μm, but we utilize only 100 nm of the spectrum from 600 to 700 nm, with an average power of ~5 mW in this band, to minimize the effects of chromatic aberration caused by the cylindrical lens in the interferometer setup. The optical layout of the line scan interferometer is shown in Fig. 21a. While the setup resembles a conventional point – scan Fourier domain-OCT system, the introduction of a cylindrical lens and 2D CCD camera enables the measurement along an entire line instead of a single point with each camera image [84]. The SC light is first collimated to an 8 mm diameter beam using a 10× objective. The collimated beam then passes through a 100 mm focal length cylindrical lens CL1 followed by an equal focal length spherical achromatic doublet L1 separated from CL1 by 200 mm. This imaging geometry transforms the 8 mm circular beam at the input of CL1 to an 8 mm long (y-axis) by 15 μm (x-axis) line at the focal plane of lens L1. The beam splitter is positioned so as to generate an identical focused line in both sample and reference arms. The beams are recombined after reflection from each arm at the beam splitter to produce an interference pattern. Neutral density filters are used to balance the light intensity in the two arms. The interference pattern is then spectrally dispersed through a

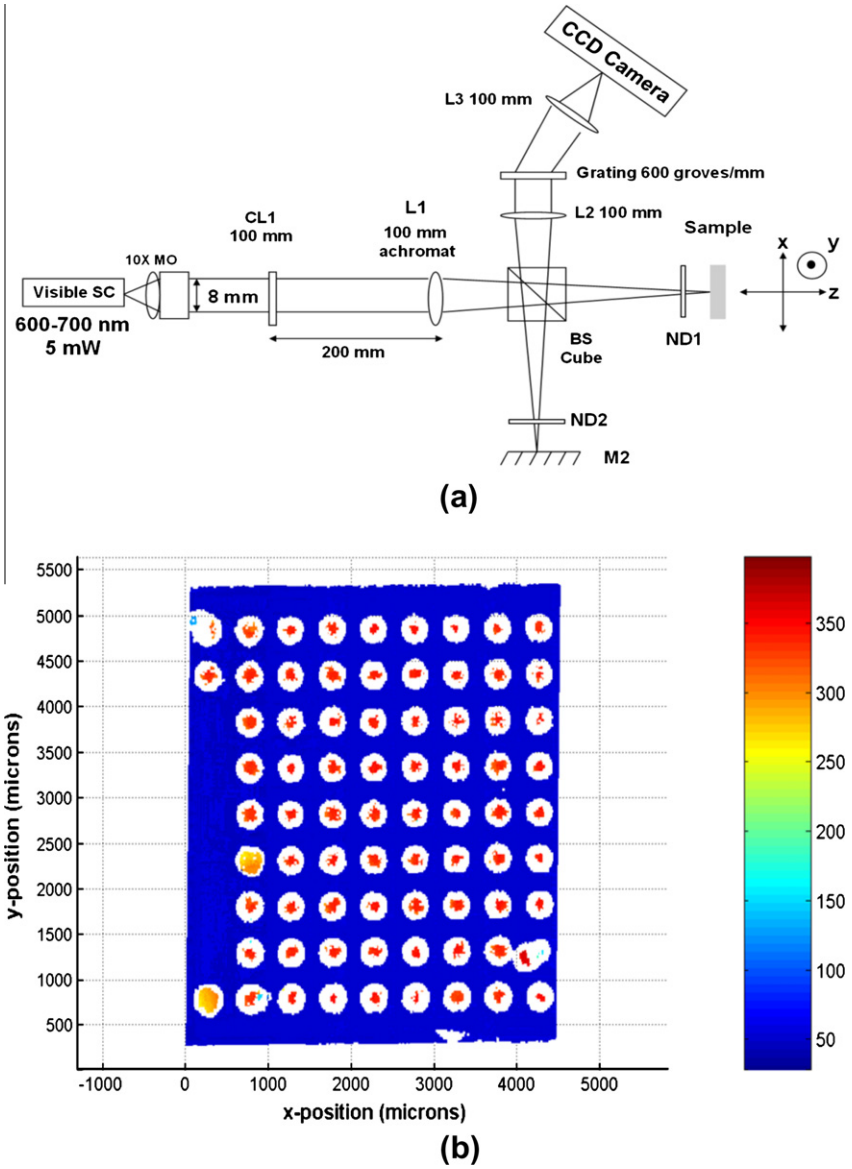

Fig. 21. (a) Experimental setup for visible SC based Fourier domain line scan interferometer, (b) 3D height map (in μm) of the solder ball grid array [82].

600 grooves/mm transmission grating and imaged on to a 2048 × 2048 pixel CCD camera. While the CCD rows contain the spatial information along the line (y-axis), the spectral information is contained along the CCD columns. Hence, a single image frame of the CCD provides height information along the entire line [85,86] and a completer 3D scan of the sample only requires 1 D translation of the sample along the x-axis.

A four step algorithm is used to extract the height information from the detected interference pattern. The first step is to do a background image subtraction by removing the dominant DC term, which is done by blocking the light in the sample arm and capturing an image with the light reflected from just the reference arm. In the next step, a sub-frame from the 2048 × 2048 pixel image is chosen to define the spatial extent of the imaged line and the spectral range of the continuum to be used for the processing. We use 768 rows corresponding to the central 5.7 mm section of the 8 mm section line and 860 columns corresponding to the 100 nm wavelength range from 600 to 700 nm. In step 3, the wavelength interferogram along each row is converted to a frequency interferogram and then re-sampled using a cubic spline interpolation algorithm [87,88] to generate 1024 equally spaced points in the frequency domain. In the final step, the result is Fourier transformed to the z space using a 32,768 point fast Fourier transform algorithm.

The transverse resolution is determined by the imaging geometry of the interferometer design. The y-resolution of the system is simply defined as being equal to the camera pixel size of 7.4 μm. The resolution along the x-axis is defined as the $1/e^2$ width of the focused line on the sample surface and is determined to be ∼15 μm. The axial resolution of the system is measured using a calibrated height standard coated with aluminum. We measure a step height of 125.2 nm ± 17.7 nm and is in close agreement with the 131 nm measured using a calibrated Dektak stylus profilometer. The maximum axial measurement range is measured to be ∼0.9 mm.

The sensitivity of the system is a measure of the smallest reflectivity of the sample arm that produces a minimum detectable SNR = 1. Assuming a shot noise limited sensitivity, we calculate the sensitivity of our system to be 75.1 dB. The experimental measurements showed a sensitivity of 70.4 dB. We attribute the deviation of 4.7 dB from the calculated value, largely to the excess relative intensity noise of the SC source above the shot-noise limit. Numerical sampling errors and mechanical vibrations in

the interferometer setup also contribute to the degraded system sensitivity. The sensitivity can be increased further by increasing the source power incident on the sample or by increasing the camera exposure time.

After characterizing the system, we perform a 3D scan of the solder ball grid array sample consisting of 75 spherical solder balls on a 4.5 mm × 4.5 mm silicon die. The solder balls are ~300 μm high with an adjacent ball spacing of ~500 μm. Fig. 21b shows the 3D map of the sample. The color bar shows the height of each pixel as measured from the interferometer zero delay plane. White areas indicate in sufficient reflected light to extract a meaningful height value. In addition to determining the ball height, the line scan system also enables the measurement of the solder ball top shape and detection of defects. While a normal ball has a round top, certain defects can alter their shape. First is the flat top and looks like a ball squished from the top indicated in the 3D image by a large number of pixels with similar average height distribution and lower average height than non-defective balls. The second defect consists of incomplete spheres, indicated by the large number of white pixels, due to the absence of reflections indicating low SNR at the location of the top of the ball. Finally, the third defect represents a ball that is positioned at the incorrect grid location, identified by determining x–y position of the ball center and comparing its distance to the neighboring balls. Fig. 22 shows the line scan 3D view of each type of defects along with the corresponding 2D image.

Thus, we demonstrate a visible SC based line scan FD interferometer with an axial resolution of ~125 nm, a lateral resolution of 15 μm and a sensitivity of 70.4 dB. The system measures a 5.7 mm × 15 μm area every 0.5 s with a typical camera exposure time of 100 μs. We measure the height and shape of ~300 μm high solder balls over an angular range of ±20°. We are able to identify solder ball shape defects such as flat top, damaged center and incorrect location. Even though our camera is capable of 15 frames per second (fps), our frame grabber card is currently limited to 2 fps. Thus, while we have sufficient source power to make measurements with just 100 μs of camera exposure time, the speed bottleneck arises for the extremely slow camera frame rate. We can achieve a faster measurement speed by using higher fps cameras and by increasing the line length of the beam incident on the sample surface. With these additions, the system could potentially be used for rapid in-line inspection of bumped wafers.

The SC average power and bandwidth requirements vary depending on the type of application. It is worth mentioning that the applications presented in our paper are performed in a laboratory setting, where we are space or equipment limited and issues like atmospheric transmission and fast acquisition times, do not play a big role. Therefore, we are limited to low power levels and/or part of the continuum bandwidth in our applications. However, in order for applications such as remote explosive detection and spectroscopy to be useful and practical, measurements need to be performed at large distances and quicker speeds. In such cases, a high average power is required to provide the necessary SNR and system sensitivity. In therapeutic applications, higher average power SC could potentially help in reducing the required treatment times. For OCT/interferometer applications, we restrict the bandwidth to ~100 nm to reduce the effects of chromatic aberrations from the available lens. However, with better optics, it is possible to use a larger bandwidth which translates to a lower coherence length and thus, a higher axial resolution.

6. Discussion and conclusions

The use of picosecond/nanosecond duration laser pump pulses along with MI induced SC generation has enabled the development of high average power broadband all-fiber SC sources. As shown by the results presented in Section 3, the architecture for MI induced SC generation shown in Fig. 1 can be used to develop SC lasers from the mid-IR to the visible wavelengths. An advantage of SC

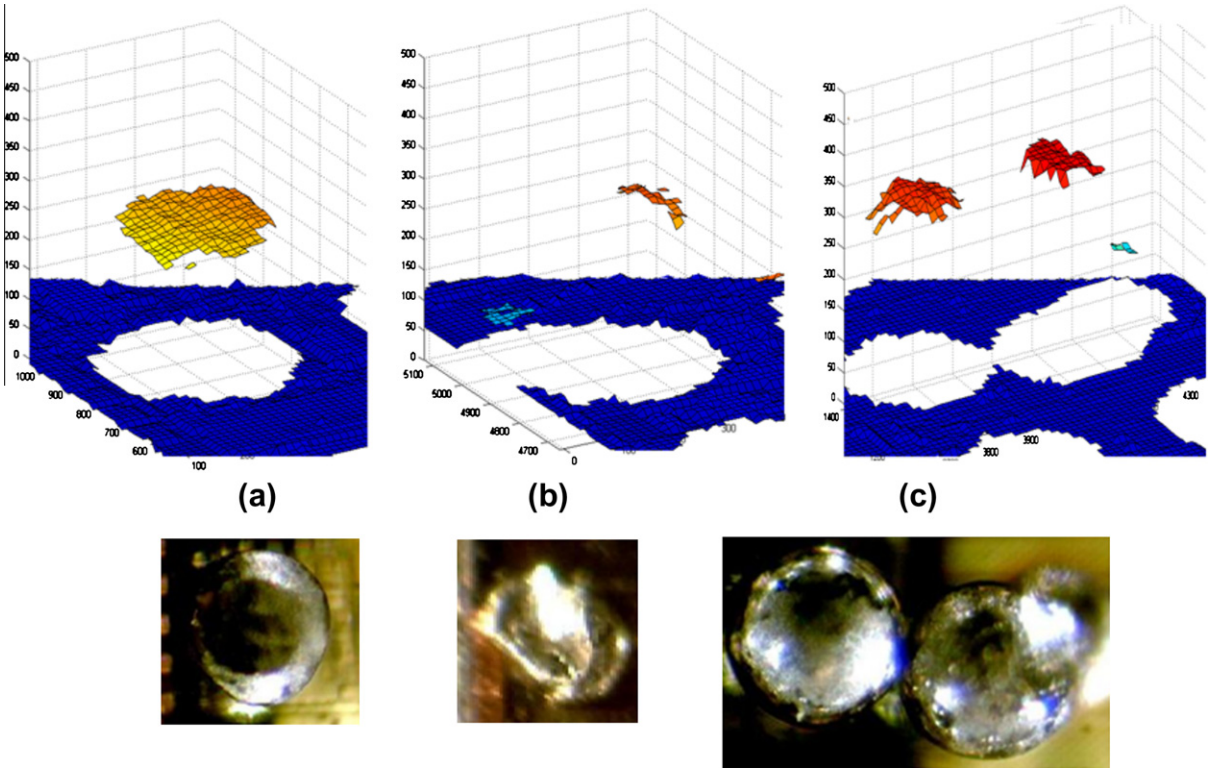

Fig. 22. 2D and 3D view of solder ball defects (a) flat top, (b) incomplete sphere, and (c) incorrect grid location [82].

generation using this framework is the scalability in time averaged power by simply increasing the repetition rate and the amplifier pump powers. For example, Fig. 4b shows that the SC average power can be continuously varied by a factor of 7.5, i.e., from 1.4 W to 10.5 W , by increasing the pulse repetition rate by the same scale from 0.42 MHz to 3.33 MHz and increasing the pump power accordingly. Compared to the conventional mode-locked lasers, the fiber SC lasers presented in this article have a greater flexibility in the system configuration from mature telecommunication technology and have potential scalability in the output power by adding more pump laser diodes. In addition, the development of high power laser diodes and cladding pumped gain fibers that can be easily spliced into the system helps to minimize coupling losses, allows better thermal management of the system and improves the over-all efficiency of the fiber SC laser sources.

To confirm that the SC in our setups is in fact initiated by MI, we measure the temporal autocorrelation and the spectrum at the output of ~3 m SMF with ~1 kW input peak power, and the results are shown in Fig. 23. In this case a 2 ns, 1.5 μm seed laser diode is amplified using erbium doped fiber amplifier stages to provide the necessary peak power. The autocorrelation result shows the formation of short pulses with a pulse envelope of ~500 fs. The spectrum is seen to have the characteristic MI sidebands around the pump, separated by the modulation frequency $\Delta\omega_{MI} = (2\gamma P_0/|\beta_2|)^{1/2}$, where γ is the nonlinearity coefficient, P_0 is the pump peak power and β_2 is the group velocity dispersion parameter of the fiber at pump wavelength. For SMF pumped by a 1 kW pump pulse at 1.55 μm, $\gamma = 1.6\ W^{-1}\ km^{-1}$, $\beta_2 = -18\ ps^2/km$, and the calculated frequency shift is ~2.12 THz. The corresponding wavelength separation is ~17 nm, which is close to the experimentally observed sidebands in Fig. 23b. We also observe that the 1530 nm MI gain peak coincides with the ASE peak from the EDFA and, thus, the pulse breakup is seeded by the ASE.

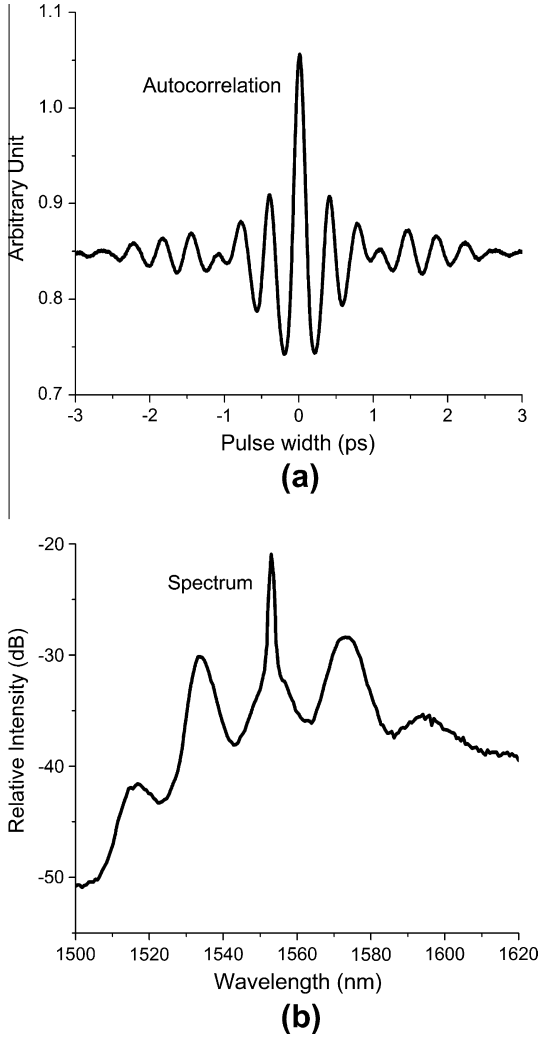

Fig. 23. MI induced pulse breakup in single mode fiber. (a) Autocorrelation and (b) spectrum. Results are shown after 3 m SMF at 1 kW input power [33].

The time averaged power of our SC setups presented in this paper is currently limited by the available pump power from the fiber amplifier. The maximum power handling of the fiber is ultimately limited by the optical material damage. For pulses shorter than ~10 ps, the optical damage can be attributed to the multi photon-initiated avalanche ionization of the target glass material as reported in [89]. For pulses from ~50 ps to 100 ns, the joule heating of the glass material needs to be taken into account [90]. In addition, the time-averaged power handling capability is primarily limited by the heating and melting of the dielectric material, such as the catastrophic destruction and fiber fuse damage, which is associated with the fiber glass melting temperature, absorption and heat conductivity [89–92]. Richardson et al. provides a comprehensive review of the current status of high power fiber lasers and discusses the key factors such as thermal management, optical nonlinearity and damage, limiting fiber laser performance in different operating regimes [93]. Therefore, such damage mechanisms put an upper limit to both the peak power of the laser pulse and the time-averaged power that the fiber can handle without incurring any damage.

For the peak power induced optical surface damage, the damage threshold scales inversely proportional to the square root of the pulse width, for pulses larger than a few tens of picoseconds. For example, the damage threshold has been measured in fused silica to be ~400 GW/cm^2 with a 10 ps pulse, and 40 GW/cm^2 with a 1 ns pulse at 1053 nm [89]. Using the reported optical damage threshold for both silica and fluoride materials [89,90], Xia et al. [50] calculate that the ZBLAN fluoride fiber with an 8.9 μm core diameter can handle >10 kW peak power with 1 ns pulse duration, while the single mode silica fiber can handle >20 kW of peak power with the same pulse width. Although, MI breakup pulses may possess higher peak power, the shortened pulse width of ~100–200 fs increases the optical damage threshold of the fibers. For the 10.5 W system presented in Section 3.1.1, the peak output power in SMF is ~6–8 kW and ~3–5 kW in ZBLAN fiber. For the modulated system presented in Section 3.1.2 with ~8 W (during the ON phase) using ~0.5 ns pulses, the peak power in SMF is ~19 kW and we estimate ~12–15 kW of peak power at the ZBLAN input, and have not yet observed any peak power induced damage at these power levels. Thus, if the peak power is kept at the same level to maintain the spectral extent, it should not be the limiting factor in the developing mid-IR fiber SC laser sources with outputs higher than 10 W, with appropriate thermal management.

The average power handling capability, on the other hand is limited by the heat absorption that results in the melting of the fiber glass. The absorption coefficient of the dielectric glass increases drastically when the temperature rises close to the glass transition temperature. The glass will then heat up, increasing the material absorption and lead to the melting of the fiber glass and catastrophic fuse damage. Therefore, the maximum average power handling capability of the fiber is limited to when the temperature of the fiber core rises close to its melting point. The melting temperature of silica glass is 1448 K with a thermal conductivity of 1.38 W/(m K) [94] and the melting temperature of ZBLAN is 528 K with a thermal conductivity of 0.628 W/(m K) [94,95]. Also, as the SC wavelength edge is pushed further into the absorption loss of ZBLAN fibers, the end of the fiber can heat up as more of

the SC is absorbed. With the assumption that ~10% of the power coupled into the SC fibers is dissipated in the SC generation process within the first meter length of the fiber, Xia et al. estimate the average power threshold for damage in SMF to be ~60 W and ~15 W in HiNL and ZBLAN (without thermal management), and that by using a 0.5 mm thick thermal pad of modest thermal conductivity (for example, 1 W/(m K)) to wrap the fiber for better thermal management, the ZBLAN threshold can be scaled up to ~40 W [50]. Thus, it should be possible to scale up the average power in ZBLAN fibers with better thermal management and heat dissipation techniques to reduce the core temperature of the fiber. Fig. 24 shows an approximate boundary of the optical damage threshold for the SC fibers used in our setups as a function of both the average and peak powers.

Studies have also been performed to understand the limitation for the SC long wavelength edge [50]. The SC long wavelength edge in ZBLAN fibers is limited by fiber nonlinearities, bend-induced loss, and fluoride material absorption. One approach to extend the SC long wavelength edge is to employ a ZBLAN fiber with a large NA as well as a reasonably small core size, which can lead to tighter confinement of the optical mode in the core region. This would allow the nonlinear wavelength generation process to be enhanced due to a smaller effective mode area and, at the same time mitigate the bend induced loss due to reduced leakage of the more tightly confined optical mode. For example, by using a step-index ZBLAN fiber with a high NA of ~0.3 and coiling the fiber around a ~60 cm diameter spool, the effect of bend induced loss is minimized based on the calculations presented in [50]. This leaves the material absorption loss as the dominant factor for restricting the long wavelength SC generation beyond ~4.5 μm. Simulation have also been reported in [51], where by shifting the loss edge of the ZBLAN fiber, a similar trend in the edge of the generated SC is observed, showing that the long wavelength edge of the SC is largely dominated by the material loss of the fiber. A possible approach for longer wavelength SC generation is to use novel fiber geometries and materials such as PCFs with higher nonlinearity. For example, SC generation extending to ~5 μm is demonstrated in a tellurite PCF with ~17 kW peak power 1.55 μm pulses coupled into an ~0.8 cm length of fiber with 50% efficiency [41]. However, a maximum average power of only ~1.12 W in a 18 μm solid core tellurite fiber has been demonstrated to date [96].

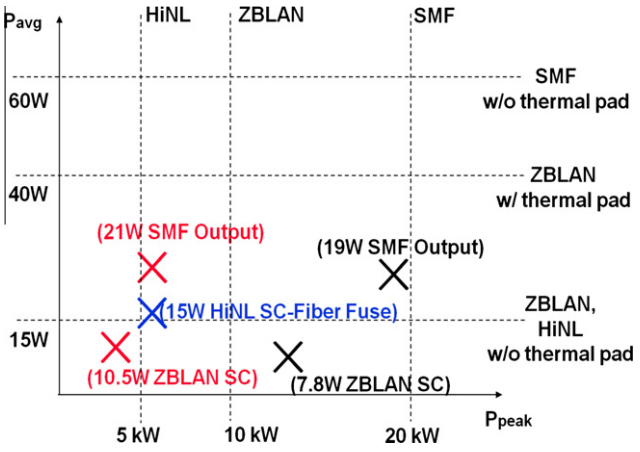

Fig. 24. Power handling estimates for various SC fibers. Crossed data points represent observed experimental data; red – Section 3.1.1, blue – Section 3.2 [50], black – Section 3.1.2. (For interpretation of the references to color in this figure legend, the reader is referred to the web version of this article.)

The mid-IR SC results presented in Section 3.1.3 suggest that the TDFA based system is capable of generating mid-IR SC with a higher efficiency than the EYFA based system. Table 3 compares the efficiency of the EYFA system in Section 3.1.2, with the TDFA system in Section 3.1.3. We observe ~1.45 times higher pump to signal conversion efficiency in the TDFA compared to the EYFA system. Also, by shifting the SC pump to ~2 μm, a longer extending spectrum is obtained compared to the EYFA system. This is beneficial for SC generation in ZBLAN fibers, since the ZDW for ZBLAN is ~1.65 μm and the TDFA system pumps the nonlinear medium in the anomalous dispersion regime, which helps to broaden the spectrum more efficiently toward longer wavelengths through the Raman processes. In comparison, SC lasers pumped in the normal dispersion regime such as the EYFA systems, initially broaden the spectrum towards either direction of the pump wavelength. We achieve ~2.5 times higher efficiency in generating wavelengths beyond 3.8 μm using the TDFA system compared to the EYFA system. However, it is worth noting that the electro-optic efficiency of the790 nm pumps are less than that of the mature 976/940 nm pumps. In addition, the 790 nm pumps also require active temperature control, such as thermoelectric cooling, which further degrade the wall plug efficiency. The 2 μm components are also not standard telecom components, and are therefore currently more expensive than components for EYFA based systems.

The mechanical splice point between the power-amp output and the ZBLAN fiber is one of the main loss components of the ZBLAN based SC systems presented in this paper and can account for as large as ~40% loss in the system. Fusion splicing the two fibers has proven to be a challenge due to the different melting temperatures of two materials. In our attempts to fusion splice silica to ZBLAN fibers, we are able to get a coupling loss of <~1 dB. However, the splice joint is very weak mechanically and could not be successfully integrated into our SC lasers. Therefore, in our systems presented in this paper, we use a mechanical coupling joint between the silica fiber and the ZBLAN fibers. Some preliminary work has also been demonstrated in fused-silica to fluoride fiber mechanical splices using a shape memory connector with losses as low as ~0.8 dB at 1550 nm [97]. Another option is to use an intermediate fiber for better match the mode profile of the SMF and ZBLAN fibers. It is also possible to increase the system efficiency by increasing the repetition rate of the seed pulses. By increasing the duty cycle of the seed pulses, higher amplifier efficiency can be achieved by reducing the losses to spontaneous emission in the gain fiber. However, operating at a higher repetition rate while maintaining the spectral extent of the SC, means

Table 3
Efficiency comparison for various components of the TDFA and EYFA based ZBLAN mid-IR SC laser.

System component	Definition		Efficiency	
	TDFA	EYFA	TDFA (%)	EYFA (%)
Pump diode electro-optic efficiency provided by manufacturer	790 nm	976 nm	~41	~50
Power-amp	2 μm Output/790 nm pump	1.54 μm output/976 nm pump	~27	~18.5
SC generation efficiency	SC output/790 nm pump	SC output/976 nm pump	~8.7	~7.5
>3.8 μm Light shifting efficiency	Power beyond 3.8 μm/790 nm pump	Power beyond 3.8 μm/976 nm pump	~2.35	~0.96

increasing the overall average power in the system, which requires more pump power and better thermal management to prevent damage to components.

In summary, we present an architecture for high power all-fiber integrated SC lasers spanning the visible to the mid-IR wavelengths (~0.45–4.5 μm). Our approach uses picosecond/nanosecond pump pulses and utilizes MI initiated pulse breakup to provide the required peak powers for broadband SC generation. In addition, we present a clear pathway for scaling up the time average power in the SC by increasing the pulse repetition rate and the pump power, while keeping the peak power, and hence, the spectral extent approximately constant. Using the presented architecture, we have scaled up the average power to ~10.5 W in a ZBLAN based SC extending from ~0.8 to 4 μm, >5 W in a near IR SC extending from ~0.8 to 2.8 μm, and >0.7 W in a visible SC extending from ~0.45 to 1.2 μm. SC modulation capability without the need for any external chopping or modulation is also demonstrated, where we generate ~3.9 W (7.8 W during modulation ON phase) in a ZBLAN SC extending from ~0.8 to 4.3 μm and modulated with a 500 Hz square wave at 50% duty cycle. In an effort to extend the SC spectrum further into the mid-IR and to improve the mid-IR SC generation efficiency, we also explore the use of a TDFA in our SC system. We observe that the mid-IR generation efficiency with respect to the amplifier pump powers can be improved by ~2.5 times in a TDFA based SC system compared to an EYFA based system. In addition, the long wavelength edge of the SC is seen to extend out further to ~4.5 μm in the TDFA based mid-IR SC laser compared to ~4.3 μm in the EYFA based SC laser. We also demonstrate various applications in metrology, health care and defense using the all-fiber SC sources described in this article. We discuss SC power handling and spectrum limitations, and possible approaches to scale up the average power and extend the SC spectrum further into the mid-IR. With the development of high power fiber coupled laser diodes, high efficiency gain fibers with increased power handling capability and adequate thermal management, it should be possible to further scale up the time average power in the fiber SC laser sources. The high average power, broad spectrum and the convenience of an all-fiber integrated laser source with near diffraction limited beam quality makes the all-fiber SC sources an attractive light source for a variety of practical applications.

Acknowledgments

The works presented here were funded by the US Army, the US Air Force, Omni Sciences Inc., Coherix Inc. and the University of Michigan. The authors would like to thank David J. Carter, James R and Michael Folts. Tice of the Physics Instrument shop at the University of Michigan, for their help in machining parts of the setup used in our experiments. The authors also thank Judy Poore and Jeff Harrison and the Histology Core of the Microscopy and Image Analysis Laboratory core facility at the University of Michigan Medical School for their help in preparing cryostat sections of the biological tissues presented in this study.

References

[1] R.R. Alfano, The Supercontinuum Laser Source: Fundamentals with Updated References, Springer-Verlag, New York, 2006.
[2] M. Kumar, M.N. Islam, J.F.L. Terry, M.J. Freeman, A. Chan, M. Neelakandan, T. Manzur, Stand-off detection of solid targets with diffuse reflection spectroscopy using a high power mid-infrared supercontinuum source, Appl. Opt. 51 (2012) 2794–2807.
[3] M. Razeghi, S. Slivken, Y. Bai, S.R. Darvish, The quantum cascade laser: a versatile and powerful tool, Opt. Photon. News 19 (2008) 42–47.
[4] R.R. Anderson, W. Farinelli, H. Laubach, D. Manstein, A.N. Yaroslavsky, J. Gubeli, K. Jordan, G.R. Neil, M. Shinn, W. Chandler, G.P. Williams, S.V. Benson, D.R. Douglas, H.F. Dylla, Selective photothermolysis of lipid-rich tissues: a free electron laser study, Lasers Surg. Med. 38 (2006) 913–919.
[5] I.T. Sorokina, K.L. Vodopyanov, Solid-State Mid-Infrared Laser Sources, Springer-Verlag, Berlin, Germany, 2003.
[6] K. Wille, Synchrotron radiation sources, Rep. Prog. Phys. 54 (1991) 1005–1067.
[7] G.S. Edwards, R.H. Austin, F.E. Carroll, M.L. Copeland, M.E. Couprie, W.E. Gabella, R.F. Haglund, B.A. Hooper, M.S. Hutson, E.D. Jansen, K.M. Joos, D.P. Kiehart, I. Lindau, J. Miao, H.S. Pratisto, J.H. Shen, Y. Tokutake, A.F.G. Van Der Meer, A. Xie, Free-electron-laser based biophysical and biomedical instrumentation, Rev. Sci. Instrum. 74 (2003) 3207–3245.
[8] J. Mandon, E. Sorokin, I.T. Sorokina, G. Guelachvili, N. Picqú, Supercontinua for high-resolution absorption multiplex infrared spectroscopy, Opt. Lett. 33 (2008) 285–287.
[9] S.A. Diddams, D.J. Jones, J. Ye, S.T. Cundiff, J.L. Hall, J.K. Ranka, R.S. Windeler, R. Holzwarth, T. Udem, T.W. Hänsch, Direct link between microwave and optical frequencies with a 300 THz femtosecond laser comb, Phys. Rev. Lett. 84 (2000) 5102–5104.
[10] G.P. Frith, D.G. Lancaster, Power scalable and efficient 790 nm pumped Tm3þ-doped fiber lasers, Proc. SPIE 610 (2) (2006) 610208.
[11] A. Carter, J. Farroni, K. Tankala, B. Samson, D. Machewirth, N. Jacobson, W. Torruellas, Y. Chen, M. Cheng, A. Galvanauskas, A. Sanchez, Robustly Single-mode Polarization Maintaining Er/Yb co-doped LMA Fiber for High Power Applications, CLEO/QELS, 2007, paper CTuS6.
[12] G. Imeshev, M. Fermann, 230 kW peak power femtosecond pulses from a high power tunable source based on amplification in Tm-doped fiber, Opt. Express 13 (2005) 7424–7431.
[13] K. Kieu, F.W. Wise, Soliton thulium-doped fiber laser with carbon nanotube saturable absorber, IEEE Photon. Technol. 21 (2009) 128–130.
[14] P.T. Rakich, Y. Fink, M. Soljačić, Efficient mid-IR spectral generation via spontaneous fifth-order cascaded-Raman amplification in silica fibers, Opt. Lett. 33 (2008) 1690–1692.
[15] M. Jiang, P. Tayebati, Stable 10 ns, kilowatt peak-power pulse generation from a gain-switched Tm-doped fiber laser, Opt. Lett. 32 (2007) 1797–1799.
[16] J.M. Dudley, G. Genty, S. Coen, Supercontinuum generation in photonic crystal fiber, Rev. Mod. Phys. 78 (2006) 1135–1184.
[17] G. Genty, S. Coen, J.M. Dudley, Fiber supercontinuum sources, J. Opt. Soc. Am. B 24 (2007) 1771–1785.
[18] J.R. Taylor, Supercontinuum Generation in Optical Fibers, Cambridge University Press, Cambridge, 2010.
[19] C. Lin, R.H. Stolen, New nanosecond continuum for excited state spectroscopy, Appl. Phys. Lett. 28 (1976) 216–218.
[20] T. Izawa, N. Shibata, A. Takeda, Optical attenuation in pure and doped fused silica in their wavelength region, Appl. Phys. Lett. 31 (1977) 33–35.
[21] A. Rulkov, M. Vyatkin, S. Popov, J. Taylor, V. Gapontsev, High brightness picosecond all-fiber generation in 525–1800 nm range with picosecond Yb pumping, Opt. Express 13 (2005) 377–381.
[22] T. Schreiber, J. Limpert, H. Zellmer, A. Tunnermann, K. Hansen, High average power supercontinuum generation in photonic crystal fibers, Opt. Commun. 228 (2003) 71–78.
[23] J.M. Stone, J.C. Knight, Visibly ''white'' light generation in uniform photonic crystal fiber using a microchip laser, Opt. Express 16 (2008) 2670–2675.
[24] A. Kudlinski, A.K. George, J.C. Knight, J.C. Travers, A. Rulkov, S. Popov, J. Taylor, Zero dispersion wavelength decreasing photonic crystal fibers for ultraviolet-extended supercontinuum, Opt. Express 14 (2006) 5715–5722.
[25] P.A. Champert, V. Couderc, P. Leproux, S. Février, V. Tombelaine, L. Labonte, P. Roy, C. Froehly, P. Nerin, White-light supercontinuum generation in normally dispersive optical fiber using original multiwavelength pumping system, Opt. Express 12 (2004) 4366–4371.
[26] C. Xiong, A. Witkowska, S.G. Leon-Saval, T.A. Birks, W.J. Wadsworth, Enhanced visible continuum generation from a microchip 1064 nm laser, Opt. Express 14 (2006) 6188–6193.
[27] W.J. Wadsworth, N. Joly, J.C. Knight, T.A. Birks, F. Biancalana, P. Russel, Supercontinuum and four-wave mixing with Q-switched pulses in endlessly single-mode photonic crystal fibres, Opt. Express 12 (2004) 299–309.
[28] C.J.S. de Matos, R.E. Kennedy, S. Popov, J.R. Taylor, 20-kW peak power all-fiber 1.57-μm source based on compression in air-core photonic bandgap fiber, its frequency doubling, and broadband generation from 430 to 1450 nm, Opt. Lett. 30 (2005) 436–438.
[29] M. Kumar, C. Xia, X. Ma, V.V. Alexander, M.N. Islam, J.F.L. Terry, C.A. Aleksoff, A. Klooster, D. Davidson, Power adjustable visible supercontinuum generation using amplified nanosecond gain-switched laser diode, Opt. Express 16 (2008) 6194–6201.
[30] J.C. Travers, Blue extension of optical fibre supercontinuum generation, J. Opt. 12 (2010) 113001.
[31] J.W. Nicholson, A.D. Yablon, P.S. WEstbrook, K.S. Feder, M.F. Yan, High power, single mode, all-fiber source of femtosecond pulses at 1550 nm and its use in supercontinuum generation, Opt. Express 12 (2004) 3025–3044.
[32] S. Moon, D.Y. Kim, Generation of octave-spanning supercontinuum with 1550 nm amplified diode-laser pulses and a dispersion-shifted fiber, Opt. Express 14 (2006) 270–278.
[33] C. Xia, M. Kumar, M.-Y. Cheng, O.P. Kulkarni, M.N. Islam, A. Galvanauskas, J.F.L. Terry, M.J. Freeman, D.A. Nolan, W.A. Wood, Supercontinuum generation in silica fibers by amplified nanosecond laser diode pulses, IEEE J. Sel. Top. Quant. Electr. 13 (2007) 789–797.
[34] A.K. Abeeluck, C. Headley, Continuous-wave pumping in the anomalous- and normal dispersion regimes of nonlinear fibers for supercontinuum generation, Opt. Lett. 30 (2005) 61–63.

[35] B.A. Cumberland, J.C. Travers, S.V. Popov, J.R. Taylor, 29 W high power CW supercontinuum source, Opt. Express 16 (2008) 5954–5962.
[36] Kang Kang Chen, Shaif-ul Alam, Jonathan H.V. Price, John R. Hayes, Dejiao Lin, Andrew Malinowski, Christophe Codemard, Debashri Ghosh, Mrinmay Pal, Shyamal K. Bhadra, David J. Richardson, Picosecond fiber MOPA pumped supercontinuum source with 39 W output power, Opt. Express 18 (2010) 5426–5432.
[37] J.S. Sanghera, I.D. Aggarwal, L.E. Busse, P.C. Pureza, V.Q. Nguyen, F.H. Kung, L.B. Shaw, F. Chenard, Chalcogenide optical fibers target midIR applications, Laser Focus World 41 (2005) 83–87.
[38] O.P. Kulkarni, C. Xia, D.J. Lee, M. Kumar, A. Kuditcher, M.N. Islam, J.F.L. Terry, M.J. Freeman, B.G. Aitken, S.C. Currie, J.E. McCarthy, M.L. Powley, D.A. Nolan, Third order cascaded Raman wavelength shifting in chalcogenide fibers and determination of Raman gain coefficient, Opt. Express 14 (2006) 7924–7930.
[39] J.S. Sanghera, L.B. Shaw, C.M. Florea, P.C. Pureza, V.Q. Nguyen, D. Gibson, F.H. Kung, and I.D. Aggarwal, Non-linearity in chalcogenide glasses and fibers and their applications, in: Quantum Electron. Laser Sci. Conf. (QELS), San Jose, CA, 2008, paper QTuL5.
[40] F.G. Omenetto, N.A. Wolchover, M.R. Wehner, M. Ross, A. Efimov, A.J. Taylor, V.V.R.K. Kumar, A.K. George, J.C. Knight, N.Y. Joly, P.S.J. Russell, Spectrally smooth supercontinuum from 350 nm to 3 μm in sub-centimeter lengths of soft-glass photonic crystal fibers, Opt. Express 14 (2006) 4928–4934.
[41] P. Domachuk, N.A. Wolchover, M. Cronin-Golomb, A. Wang, A.K. George, C.M.B. Cordeiro, J.C. Knight, F.G. Omenetto, Over 4000 nm bandwidth of mid-IR supercontinuum generation in sub-centimeter segments of highly nonlinear tellurite PCFs, Opt. Express 16 (2008) 7161–7168.
[42] J. Hu, C.R. Menyuk, L.B. Shaw, J.S. Sanghera, I.D. Aggarwal, Maximizing the bandwidth of supercontinuum generation in As_2Se_3 chalcogenide fibers, Opt. Express 18 (2010) 6722–6739.
[43] Z. Chen, A.J. Taylor, A. Efimov, Coherent mid-infrared broadband continuum generation in non-uniform ZBLAN fiber taper, Opt. Express 17 (2009) 5852–5860.
[44] J.H.V. Price, T.M. Monro, H. Ebendorff-Heidepriem, F. Poletti, P. Horak, V. Finazzi, J.Y.Y. Leong, P. Petropoulos, J.C. Flanagan, G. Brambilla, X. Feng, D.J. Richardson, Mid-IR supercontinuum generation from nonsilica microstructured optical fibers, IEEE J. Quantum. Electron. 13 (2007) 738–749.
[45] X. Zhu, N. Peyghambarian, High-power ZBLAN Glass fiber lasers: review and prospect, Adv. OptoElectron. 2010 (2010) 1–23.
[46] C.L. Hagen, J.W. Walewski, S.T. Sanders, Generation of a continuum extending to the midinfrared by pumping ZBLAN fiber with an ultrafast 1550-nm source, IEEE Photon. Technol. Lett. 18 (2006) 91–93.
[47] G. Qin, X. Yan, C. Kito, M. Liao, C. Chaudhari, T. Suzuki, Y. Ohishi, Ultrabroadband supercontinuum generation from ultraviolet to 6.28 μm in a fluoride fiber, Appl. Phys. Lett. 95 (2009) 161103.
[48] C. Xia, M. Kumar, O.P. Kulkarni, M.N. Islam, J.F.L. Terry, M.J. Freeman, M. Poulain, G. Maze, Mid-infrared supercontinuum generation to 4.5 μm in ZBLAN fluoride fibers by nanosecond diode pumping, Opt. Lett. 31 (2006) 2553–2555.
[49] C. Xia, M. Kumar, M.-Y. Cheng, R.S. Hegde, M.N. Islam, A. Galvanauskas, J.F.L. Terry, M. Poulain, G. Maze, Power scalable mid-infrared supercontinuum generation in ZBLAN fluoride fibers with up to 1.3 W time-averaged power, Opt. Express 15 (2007) 865–871.
[50] C. Xia, Z. Xu, M.N. Islam, J.F.L. Terry, M.J. Freeman, A. Zakel, J. Mauricio, 10.5 W time-averaged power mid-IR supercontinuum generation extending beyond 4 μm with direct pulse pattern modulation, IEEE J. Sel. Top. Quant. Electron. 15 (2009) 422–434.
[51] O.P. Kulkarni, V.V. Alexander, M. Kumar, M.J. Freeman, M.N. Islam, J.F.L. Terry, M. Neelakandan, A. Chan, Supercontinuum generation from ~1.9 to 4:5 μm in ZBLAN fiber with high average power generation beyond 3:8 μm using a thulium-doped fiber amplifier, J. Opt. Soc. Am. B 28 (2011) 2486–2498.
[52] J. Geng, Qi Wang, S. Jiang, High-spectral-flatness mid-infrared supercontinuum generated from a Tm-doped fiber amplifier, Appl. Opt. (2011).
[53] G.P. Agrawal, Nonlinear Fiber Optics, third ed., Academic, San Diego, CA, 2001.
[54] J.R. Taylor, Optical Solitons: Theory and Experiment, Cambridge University Press, Cambridge, 1992.
[55] D.V. Skryabin, A.V. Gorbach, Colloquium: looking at a soliton through the prism of optical supercontinuum, Rev. Mod. Phys. 82 (2010) 1287–1299.
[56] E.M. Dianov, Z.S. Nikanova, A.M. Prokhorov, V.N. Serkin, Optimal compression of multi-soliton pulses in optical fibers, Sov. Technol. Phys. Lett. 12 (1986) 311–313.
[57] G. Genty, Minna Surakka, Jari Turunen, Ari T. Friberg, Complete characterization of supercontinuum coherence, J. Opt. Soc. Am. B 28 (2011) 2301–2309.
[58] J.A. Harrington, Infrared Fibers and their Applications, SPIE, 2004.
[59] M.P. Fuller, P.R. Griffiths, Diffuse reflectance measurements by infrared Fourier transform spectroscopy, Anal. Chem. 50 (1978) 1906–1910.
[60] J.L. Gottfried, F.C.D. Lucia Jr., C.A. Munson, A.W. Miziolek, Laser induced breakdown spectroscopy for detection of explosives residues: a review of recent advances, challenges and future prospects, Anal. Bioanal. Chem. 395 (2009) 283–300.
[61] G. Comanescu, C.K. Manka, J. Grun, S. Nikitin, D. Zabetakis, Identification of explosives with two-dimensional ultraviolet resonance Raman spectroscopy, Appl. Spectrosc. 62 (2008) 833–839.
[62] H. Li, D.A. Harris, B. Xu, P.J. Wrzesinski, V.V. Lozovoy, M. Dantus, Standoff and arms-length detection of chemicals with single-beam coherent anti-Stokes Raman scattering, Appl. Opt. 48 (2009) B17–B22.
[63] A. Savitzky, M. Golay, Smoothing and differentiation of data by simplified least squares procedures, Anal. Chem. 44 (1964) 1627–1638.
[64] S.V. Ingale, P.U. Sastry, A.K. Patra, R. Tewari, P.B. Wagh, S.C. Gupta, Micro structural investigations of TNT and PETN incorporated silica xerogels, J. Sol–Gel Sci. Technol. 54 (2010) 238–242.
[65] A. Banas, K. Banas, M. Bahou, H.O. Moser, L. Wen, P. Yang, Z.J. Li, M. Cholewa, S.K. Lim, Ch.H. Lim, Post-blast detection of traces of explosives by means of Fourier transform infrared spectroscopy, Vib. Spectrosc. 51 (2009) 168–176.
[66] J. Janni, B.D. Gilbert, R.W. Field, J.I. Steinfeld, Infrared absorption of explosive molecule vapors, Spectrochim. Acta Part A 53 (1997) 1375–1381.
[67] K. Ke, C. Xia, M.N. Islam, M.J. Welsh, M.J. Freeman, Mid-infrared absorption spectroscopy and differential damage in vitro between lipids and proteins by an all-fiber-integrated supercontinuum laser, Opt. Express 17 (2009) 12627–12640.
[68] P. Libby, Atherosclerosis: the new view, Sci. Am. 286 (2002) 47–55.
[69] K.A. Tillman, R.R.J. Maier, D.T. Reid, E.D. McNaghten, Mid-infrared absorption spectroscopy across a 14.4 THz spectral range using a broadband femtosecond optical parametric oscillator, Appl. Phys. Lett. 85 (2004) 3366–3368.
[70] E. Sorokin, I.T. Sorokina, J. Mandon, G. Guelachvili, N. Picqué, Sensitive multiplex spectroscopy in the molecular fingerprint 2.4 μm region with a Cr^{2+}:ZnSe femtosecond laser, Opt. Express 15 (2007) 16540–16545.
[71] H.-Y.N. Holman, K.A. Bjornstad, M.C. Martin, W.R. McKinney, E.A. Blakely, F.G. Blankenberg, Midinfrared reflectivity of experimental atheromas, J. Biomed. Opt. 13 (2008) 030503.
[72] K. Awazu, A. Nagai, K. Aizawa, Selective removal of cholesterol esters in an arteriosclerotic region of blood vessels with a free-electron laser, Lasers Surg. Med. 23 (1998) 233–237.
[73] V.V. Alexander, K. Ke, Z. Xu, M.N. Islam, M.J. Freeman, B. Pitt, M.J. Welsh, J.S. Orringer, Photothermolysis of sebaceous glands in human skin ex vivo with a 1708 nm Raman fiber laser and contact cooling, Lasers Surg. Med. 43 (2011) 470–480.
[74] C. Paluszkiewicz, W.M. Kwiatek, A. Banas, A. Kisiel, A. Marcelli, A. Piccinini, SR-FTIR spectroscopic preliminary findings of non-cancerous, cancerous, and hyperplastic human prostate tissues, Vib. Spectrosc. 43 (2007) 237–242.
[75] B.A. Hooper, A. Maheshwari, A.C. Curry, T.M. Alter, Catheter for diagnosis and therapy with infrared evanescent waves, Appl. Opt. 42 (2003) 3205–3214.
[76] J.M. Gentner, E. Wentrup-Byrne, P.J. Walker, M.D. Walsh, Comparison of fresh and post-mortem human arterial tissue: an analysis using FT-IR microspectroscopy and chemometrics, Cell Mol. Biol. (Noisy-le-grand) 44 (1998) 251–259.
[77] V.V. Alexander, H. Deng, M.N. Islam, J.F.L. Terry, R.B. Pittman, T. Valen, Surface roughness measurement of flat and curved machined metal parts using a near infrared super-continuum laser, Opt. Eng. 50 (2011) 113602.
[78] E.P. DeGarmo, J.T. Black, R.A. Kohser, Materials and Processes in Manufacturing, Prentice-Hall, Englewood Cliffs, NJ, 1997.
[79] S. Adachi, K. Horio, Y. Nakamura, K. Nakano, A. Tanke, Development of Toyota 1ZZ-FE Engine, SAE Technical Paper Series 981087, 1998.
[80] S. Tung, M.L. McMillan, Automotive tribology overview of current advances and challenges for the future, Tribol. Int. 37 (2004) 517–536.
[81] P. Beckmann, A. Spizzichino, The Scattering of Electromagnetic Waves from Rough Surfaces, Pergamon, New York, 1963.
[82] M. Kumar, M.N. Islam, J.F.L. Terry, C.A. Aleksoff, D. Davidson, High resolution line scan interferometer for solder ball inspection using a visible supercontinuum source, Opt. Express 18 (2010) 22471–22484.
[83] A. Ishii, J. Mitsudo, Constant-magnification varifocal mirror and its application to measuring three-dimensional (3-D) shape of solder bump, IEICE Trans. Electron. E 90 (2007) 6–11.
[84] T. Endo, Y. Yasuno, S. Makita, M. Itoh, T. Yatagai, Profilometry with line-field Fourier-domain interferometry, Opt. Express 13 (2005) 695–701.
[85] Y. Yasuno, T. Endo, S. Makita, G. Aoki, M. Itoh, T. Yatagai, Three-dimensional line-field Fourier domain optical coherence tomography for in vivo dermatological investigation, J. Biomed. Opt. 11 (2006) 014014.
[86] Y. Nakamura, S. Makita, M. Yamanari, M. Itoh, T. Yatagai, Y. Yasuno, High-speed three-dimensional human retinal imaging by line-field spectral domain optical coherence tomography, Opt. Express 15 (2007) 7103–7116.
[87] C. Dorrer, N. Belabas, J.-P. Likforman, M. Joffre, Spectral resolution and sampling issues in Fourier-transform spectral interferometry, J. Opt. Soc. Am. B 17 (2000).
[88] M. Choma, M. Sarunic, C. Yang, J. Izatt, Sensitivity advantage of swept source and Fourier domain optical coherence tomography, Opt. Express 11 (2003) 2183–2189.
[89] B.C. Stuart, M.D. Feit, S. Herman, A.M. Rubenchik, B.W. Shore, M.D. Perry, Optical ablation by high-power short-pulse lasers, J. Opt. Soc. Am. B 13 (1996) 459–468.
[90] B.C. Stuart, M.D. Feit, S. Herman, A.M. Rubenchik, B.W. Shore, M.D. Perry, Nanosecond-to-femtosecond laser-induced breakdown in dielectrics, Phys. Rev. B 53 (1996) 1749–1761.
[91] S.I. Yakovlenko, Physical processes upon the optical discharge propagation in optical fiber, Laser Phys. 16 (2006) 1273–1290.
[92] E.M. Dianov, I.A. Bufetov, A.A. Frolov, V.M. Mashinsky, V.G. Plotnichenko, M.F. Churbanov, G.E. Snopatin, Catastrophic destruction of fluoride and chalcogenide optical fibres, Electron. Lett. 38 (2002) 783–784.
[93] D.J. Richardson, J. Nilsson, W.A. Clarkson, High power fiber lasers: current status and future perspectives, J. Opt. Soc. Am. B 27 (2010) B63–B92 (Invited).
[94] J.M. Parker, Fluoride glasses, Annu. Rev. Mater. Sci. 19 (1989) 21–41.

[95] J.A. Harrington, Infrared fibers, in: M. Bass, J.M. Enoch, E.W. Van Striland, W.L. Wolfe (Eds.), Handbook of Optics, Classical, Vision & X-ray Optics, vol. 3, Optical Society of America, Washington, DC, 2002, pp. 14.1–14.16.
[96] K. Li, G. Zhang, L. Hu, Watt-level ~2 μm laser output in Tm3p-doped tungsten tellurite glass double-cladding fiber, Opt. Lett. 35 (2010) 4136–4138.
[97] A. Lyakh, C. Pflügl, L. Diehl, Q.J. Wang, F. Capasso, X.J. Wang, J.Y. Fan, T. Tanbun-Ek, R. Maulini, A. Tsekoun, R. Go, C. Kumar, N. Patel, 1:6 W high wall plug efficiency, continuous-wave room temperature quantum cascade laser emitting at 4.6 μm, Appl. Phys. Lett. 92 (2008) 111110.